Article

Intratumoral delivery of lipid nanoparticle-formulated mRNA encoding IL-21, IL-7, and 4-1BBL induces systemic anti-tumor immunity

Ahmed E. I. Hamouda [1,2], Jessica Filtjens[3,12], Elisabeth Brabants[3,12], Daliya Kancheva [1,2], Ayla Debraekeleer[1,2], Jan Brughmans[1,2], Lotte Jacobs[3], Pauline M. R. Bardet [1,2], Elisabeth Knetemann [4], Pierre Lefesvre[5], Lize Allonsius [1,2], Mark Gontsarik [6], Ismael Varela [3], Marian Crabbé[3], Emile J. Clappaert[1,2,7], Federica Cappellesso[1,2], Aarushi A. Caro[1,2,8], Alícia Gordún Peiró [1,2,8], Luna Fredericq[1,2,7], Eva Hadadi[1,2,7], Mariona Estapé Senti[9], Raymond Schiffelers [9], Leo A. van Grunsven [4], Frank Aboubakar Nana[10,11], Bruno G. De Geest [6], Sofie Deschoemaeker [1,2], Stefaan De Koker[3], Florence Lambolez[3,13] ✉ & Damya Laoui [1,2,13] ✉

Local delivery of mRNA-based immunotherapy offers a promising avenue as it enables the production of specific immunomodulatory proteins that can stimulate the immune system to recognize and eliminate cancer cells while limiting systemic exposure and toxicities. Here, we develop and employ lipid-based nanoparticles (LNPs) to intratumorally deliver an mRNA mixture encoding the cytokines interleukin (IL)−21 and IL-7 and the immunostimulatory molecule 4-1BB ligand (Triplet LNP). IL-21 synergy with IL-7 and 4-1BBL leads to a profound increase in the frequency of tumor-infiltrating CD8^{+} T cells and their capacity to produce granzyme B and IFN-γ, leading to tumor eradication and the development of long-term immunological memory. Mechanistically, the efficacy of the Triplet LNP depends on tumor-draining lymph nodes to tumor CD8^{+} T-cell trafficking. Moreover, we highlight the therapeutic potential of the Triplet LNP in multiple tumor models in female mice and its superior therapeutic efficacy to immune checkpoint blockade. Ultimately, the expression of these immunomodulators is associated with better overall survival in patients with cancer.

Therapeutic mRNA is a versatile and precise tool that can be exploited against a wide range of diseases, including cancer[1,2]. mRNA encoding immunostimulatory proteins, such as cytokines and costimulatory molecules, can boost immune effector cells to target and eradicate cancer cells. Intratumoral administration of therapeutic mRNA increases the concentration of immunostimulatory proteins within the tumor microenvironment (TME), inducing potent anti-tumor responses in preclinical tumor models, while reducing systemic exposure and hence toxicity[3–6]. Nonetheless, poor translation efficiency of naked mRNA remains a challenge due to its instability, high susceptibility to degradation by ribonucleases, and limited cellular uptake[7]. The encapsulation of therapeutic mRNA in lipid-based nanoparticles

1

(LNPs) can overcome these issues, improving its translation efficiency within the TME and overall therapeutic efficacy[5,6,8,9].

Interleukin (IL)−21, a member of the common γ-chain cytokine family, modulates diverse immune cell subsets, including T cells, B cells, natural killer (NK) cells, macrophages, monocytes, and dendritic cells (DCs)[10]. IL-21 was shown to promote NK and T-cell proliferation and regulate their effector functions including their cytotoxic capacity and secretion of interferon (IFN)-γ, eliciting anti-tumor responses in multiple preclinical tumor models[11–16]. In these studies, either recombinant IL-21[11–14] or oncolytic viruses armed with IL-21[15,16] were used. Recombinant IL-21 exhibits a short half-life of 0.2 h in mice[17] and 2 h in humans[18], which has limited its therapeutic efficacy in clinical trials[19]. On the other hand, the use of viral vectors is associated with the risk of insertional mutagenesis and the development of anti-vector immunity, preventing their repeated administration. Moreover, the use of IL-21 as a monotherapy does not result in optimal therapeutic responses, and combinations with chemotherapeutics, the immune checkpoint blocker (ICB) anti-PD1, or anti-T-cell immunoglobulin and mucin domain (TIM) 3 were necessary to elevate its efficacy[13,14]. Local administration of IL-21-encoding mRNA can be a beneficial approach since mRNA is safe, transient, easier to manufacture, and can be administered repeatedly[1,2]. Additionally, the therapy can be tailored by combining IL-21-encoding mRNA with an mRNA mixture encoding potentially synergistic immunomodulators, thus optimizing its therapeutic efficacy.

IL-7, another member of the common γ-chain cytokine family, plays a pivotal role in naïve CD8+ T-cell development and survival, and homeostatic proliferation in the periphery[20,21]. IL-7 was also shown to induce naïve CD8+ T-cell differentiation towards a memory phenotype and enhance their effector functions[22,23]. Within the TME, IL-7 can protect CD8+ T cells against adenosine-mediated immunosuppression, thus promoting anti-tumor effects[24]. However, systemic administration of recombinant IL-7 monotherapy had no benefits in patients with cancer despite a notable increase in circulating CD8+ T cells[25,26], which is presumably due to a general expansion of IL-7 receptor+ CD8+ T cells, most of which are not tumor-specific[27].

4-1BB, a member of the tumor necrosis factor (TNF) receptor family, is transiently induced on CD8+ T cells following T-cell receptor (TCR) stimulation, which upon binding to its ligand (4-1BBL), initiates a signaling cascade that leads to enhanced CD8+ T-cell proliferation, cytotoxic capacity, and cytokine production[28]. Systemic administration of 4-1BB agonist antibodies conferred encouraging anti-tumor responses, however, its clinical efficacy is hampered due to severe dose-limiting hepatotoxicity[29–32].

In this study, we demonstrate the capacity of our LNPs to transfect human and murine cells and the therapeutic efficacy of intratumorally administered LNPs carrying nucleoside-modified mRNA encoding IL-21, IL-7, and 4-1BBL against treated and distal tumors. In addition, the Triplet LNP treatment can resensitize resistant tumor models to anti-PD1. Using high-dimensional flow cytometry and single-cell RNA and surface protein co-profiling, we assess the effects of the Triplet LNP on the immune cell composition and activation status within the TME. Finally, we show that the Triplet LNP treatment induces tumor-specific CD8+ T cells and immunological memory that protects against tumor rechallenge.

Results

Intratumoral injection of LNP-formulated mRNA leads to efficient protein expression in myeloid and cancer cells

Lipid-based nanoparticles are highly effective carriers to enhance mRNA delivery in vivo. The ionizable lipid is considered the most critical component within the LNP, as it mediates mRNA encapsulation and the efficiency of endosomal escape. Recently, we have reported the design of the ionizable cationic lipid S-Ac7-DOG that combines improved expression levels with reduced reactogenicity upon intramuscular injection (Supplementary Fig. 1A)[33,34]. To evaluate whether LNP-mediated mRNA delivery using the same LNP composition leads to the expression of the target protein in vitro, we developed and characterized LNPs carrying mRNA encoding the cell surface glycoprotein thymus cell antigen 1a (Thy1.1) (Supplementary Fig. 1B). We then transfected the MC38 colon carcinoma cell line with the LNP-formulated Thy1.1 mRNA and quantified Thy1.1 expression after one day using flow cytometry. Thy1.1 LNP transfected MC38 cells and induced Thy1.1 expression in almost 100% of MC38 cells (Supplementary Fig. 1C). To assess the in vivo biodistribution of the target protein and whether LNP-mediated mRNA delivery enhanced its expression relative to naked mRNA, we injected subcutaneous MC38 colon carcinoma tumors with either mRNA encoding the firefly luciferase (FLuc mRNA) or LNPs carrying the firefly luciferase mRNA (FLuc LNP). Intratumoral delivery of LNP-formulated FLuc mRNA induced higher luciferase activity than that of naked FLuc mRNA as analyzed by in vivo bioluminescent imaging (Fig. 1A). However, as previously reported[35], accumulation of FLuc LNP was also observed in the liver, albeit to a lower extent than in the tumor (Fig. 1A). Next, we sought to identify the cells expressing the target protein within the TME. To this end, we injected either naked or LNP-formulated Thy1.1 mRNA intratumorally into subcutaneous MC38 tumors and quantified Thy1.1 expression after one day using flow cytometry (Fig. 1B). LNP mediated Thy1.1 mRNA delivery resulted in increased expression compared to naked Thy1.1 mRNA in both CD45+ (immune) and CD45- (non-immune) cells (Fig. 1C). Within the CD45+ compartment, Thy1.1 expression was restricted to CD11b+ myeloid cells and in particular to tumor-associated macrophages (TAMs), monocytes, and conventional dendritic cells type 2 (cDC2s) (Fig. 1D and Supplementary Fig. 1D). Here, we defined three different subsets of TAMs, based on their expression of major histocompatibility complex (MHC)-II and macrophage mannose receptor (MMR), the latter marker being associated with an M2-like phenotype, and found that MMR+ TAMs were enriched within the Thy1.1+ TAMs (Supplementary Fig. 1E). Accordingly, Thy1.1 expression was higher in M2-polarized bone marrow-derived macrophages (BMDM) compared to M1-polarized BMDMs incubated with Thy1.1 mRNA LNPs (Supplementary Fig. 1F). Since TAMs and monocytes are the most abundant myeloid cells within MC38 tumors (Supplementary Fig. 1G), we speculated that their high frequency within the Thy1.1+ compartment could be merely due to their high abundance in the TME rather than their superior capacity to take up the LNPs. To take this into account, we quantified the frequency of Thy1.1+ cells within TAMs, monocytes, and cDC2s and found that cDC2s showed the highest intrinsic uptake capacity of the Thy1.1 LNP and consequent Thy1.1 protein expression (Fig. 1E). To assess whether LNP uptake impacts cDC2 activation, we determined the expression of several cDC activation markers including CCR7, CD80, CD40, CD83, programmed cell death ligand (PD-L) 1, and MHC-II in Thy1.1+ and Thy1.1- cDC2s (Fig. 1F, G and Supplementary Fig. 1H–K). CCR7 and CD80 levels increased significantly in Thy1.1+ cDC2s, suggesting that LNP uptake and mRNA translation might induce cDC2 activation and migration toward the tumor-draining lymph node (tdLN). In this respect, we observed that in the tdLN, cDC2s were the most abundant Thy1.1+ cells and that approximately 90% of Thy1.1+ cDC2s in the tdLN had a migratory phenotype (CD11c^int MHC-II^hi CCR7+), suggesting that they might have migrated from the tumor to the tdLN upon taking up the Thy1.1 LNP (Fig. 1H and Supplementary Fig. 1L). Importantly, the frequency of Thy1.1+ cells in the tdLN and spleen was drastically lower compared to that of the tumor (Fig. 1I), indicating limited leakage of Thy1.1 LNP into the secondary lymphoid tissues. Of note, we identified a minor population of Thy1.1+ CD19+ B cells in the tdLN and spleen, which was similarly observed in vehicle-treated mice; therefore, we excluded this population from our analysis (Supplementary Fig. 1M). Next, we
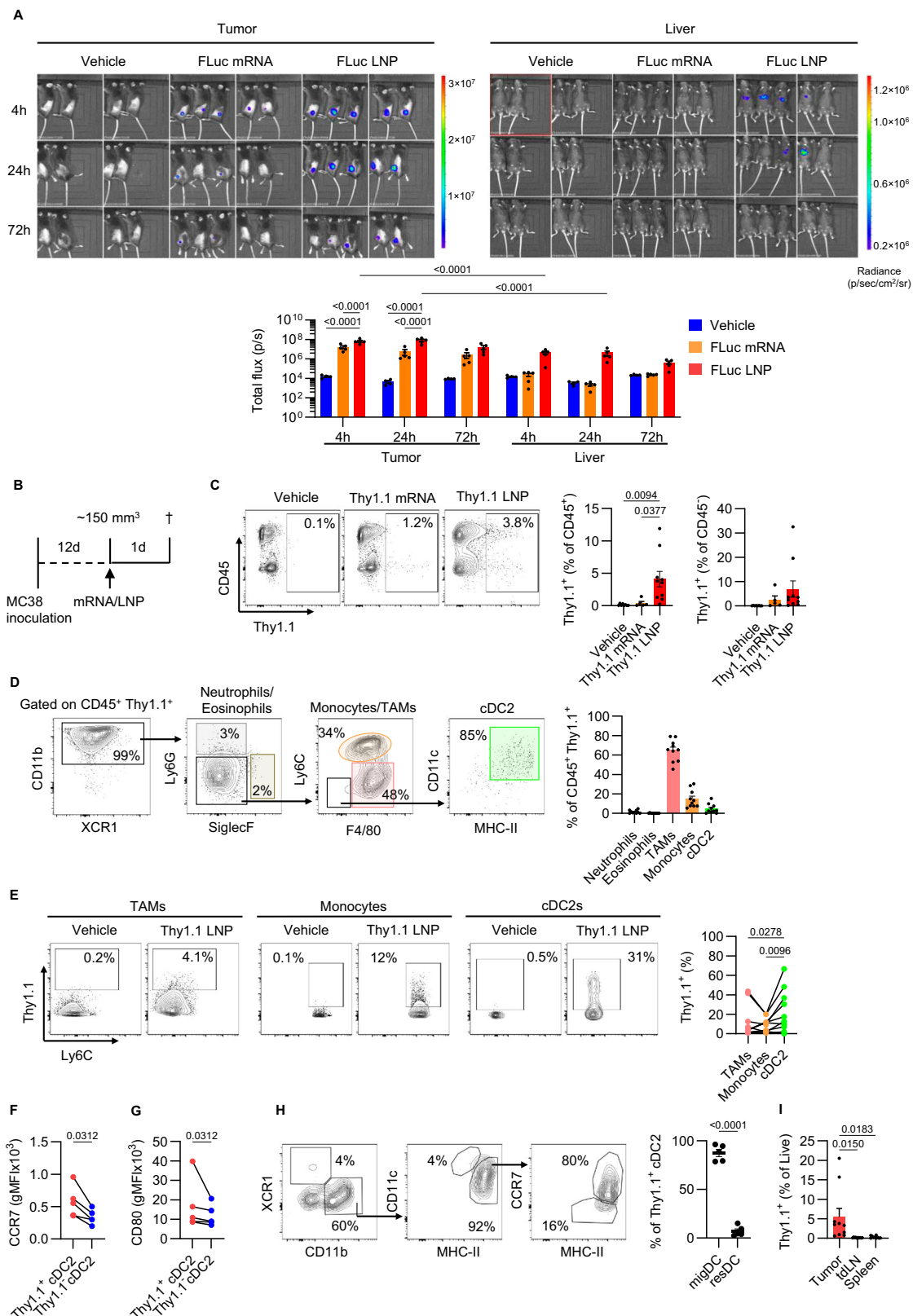
injected Thy1.1 LNP intratumorally into subcutaneous MC38 tumors to assess the relative Thy1.1 expression in the liver one day after the injection (Fig. 1B). The frequency of Thy1.1$^+$ cells in the liver was significantly lower than in the tumor (Supplementary Fig. 2A). In the liver, Thy1.1$^+$ cells were mostly CD45$^+$ myeloid cells, particularly monocytes, neutrophils and to a lower extent Kupffer cells (Supplementary Fig. 2B–E).

Triplet LNP eradicates tumors across multiple preclinical models

Having demonstrated that mRNA delivery via LNPs elicited a higher protein expression than naked mRNA in tumors, we sought to assess the therapeutic potential of LNPs carrying mRNA encoding immunostimulatory proteins. Given the reported anti-tumor efficacy of IL-21[11–16], we first developed LNPs carrying IL-21 mRNA. Following a single

Fig. 1 | Intratumoral injection of LNP-formulated mRNA leads to efficient protein expression by myeloid and cancer cells. A Images and bar graph show in vivo bioluminescence of luciferin over 72 h in MC38 tumor following a single intratumoral administration of vehicle ($n = 4$ animals), naked luciferase mRNA ($n = 5$ animals) or LNP-formulated luciferase mRNA ($n = 5$ animals). **B** Schematic outline of experimental procedures. **C** Representative flow cytometry plots and bar graphs show the frequency of Thy1.1$^+$ CD45$^+$ and Thy1.1$^+$ CD45$^-$ cells in subcutaneous MC38 tumors 24 h post intratumoral injection of vehicle ($n = 8$ animals), naked Thy1.1 mRNA ($n = 5$ animals), or Thy1.1 LNP ($n = 10$ animals). **D** Gating strategy and bar graph show the frequency of myeloid cell subsets within Thy1.1$^+$ CD45$^+$ cells in the tumor ($n = 10$ animals). **E** Representative flow cytometry plots and graph show the frequency of Thy1.1$^+$ cells within TAMs, monocytes, and cDC2s in the tumor ($n = 10$ animals). Graphs show gMFI of (**F**) CCR7 and (**G**) CD80 in Thy1.1$^+$ and Thy1.1$^-$ cDC2s

in the tumor ($n = 5$ animals). **H** Representative flow cytometry plots and scatter plot show the frequency of migDC and resDC within Thy1.1$^+$ cDC2s in the tdLN ($n = 5$ animals). **I** Bar graph shows the frequency of live Thy1.1$^+$ cells in the tumor, tdLN, and spleen ($n = 10$ animals). Bars and horizontal lines show mean. Error bars indicate SEM. **A** Two-way ANOVA followed by Šídák's multiple comparisons test, **C, I** one-way ANOVA followed by post hoc Tukey's multiple comparisons test, **E** repeated measures one-way ANOVA followed by Holm-Šídák's multiple comparisons test, **F, G** one-tailed Wilcoxon matched pairs signed rank test and (**H**) one-tailed unpaired t test were performed. Data shown in (**B-D**), and (**H**) are pooled from two independent experiments. Source data are provided as a Source Data file. gMFI, geometric mean fluorescence intensity; SEM, standard error of mean; TAMs, tumor-associated macrophages; tdLN, tumor-draining lymph nodes.

intratumoral injection of IL-21 LNP, we observed a profound increase in the protein levels of IL-21 in the tumor and serum presumably due to its leakage from the tumor into the circulation (Fig. 2A, B and Supplementary Fig. 3A). Three intratumoral injections of IL-21 LNP showed a moderate efficacy against MC38 tumors, inducing complete tumor regression in 4 out of 8 mice (Supplementary Fig. 3B, C). To enhance the therapeutic efficacy of IL-21, we sought to combine it with other potentially synergistic immunostimulatory molecules. IL-7 has been shown to synergize with IL-21 in vitro and in vivo, promoting CD8$^+$ T-cell proliferation and cytotoxicity[36–38]. 4-1BB has emerged as an attractive immunotherapy target amongst other molecules, such as OX40 and CD27, due to its role in enhancing CD8$^+$ T-cell survival and cytokine production[28]. To this end, we developed LNPs carrying either IL-7 or 4-1BBL mRNA and assessed their protein levels in the tumor and serum post a single intratumoral injection (Fig. 2A, C, D and Supplementary Fig. 3D, E). Next, we evaluated the therapeutic efficacy of IL-21, IL-7 and 4-1BBL LNPs alone and their combinations to assess their potential synergy (Fig. 2E, F). While IL-21 LNP as a monotherapy was able to abrogate MC38 tumor growth in 3 out of 7 mice, IL-7 and 4-1BBL alone had no effect on tumor growth. IL-7 synergized with IL-21 and resulted in complete tumor regression in 5 out of 7 mice (Fig. 2F). In contrast, in IL-21/4-1BBL LNP-treated mice, only 1 out of 7 mice showed complete tumor regression, suggesting a potentially lower anti-tumor activity compared to IL-21 alone (Fig. 2F). Interestingly, mice treated with IL-7/4-1BBL LNP showed delayed tumor growth in comparison to IL-7 and 4-1BBL monotherapies and completely abrogated tumor growth in 1 out of 7 mice (Fig. 2F). More importantly, the combination of IL-21, IL-7 and 4-1BBL (i.e. Triplet LNP) showed the highest therapeutic efficacy and led to 6 out of 7 complete regressors (Fig. 2F).

Having demonstrated the therapeutic efficacy of the Triplet LNP in the MC38 tumor model, we sought to assess its efficacy in ICB-resistant models. Triple-negative breast cancer (TNBC) is an aggressive disease with a poor prognosis due to its limited response to the available therapeutic options, including ICB[39]. Therefore, we evaluated the therapeutic efficacy of IL-21 LNP, IL-7 LNP, 4-1BBL LNP, IL-21/IL-7 LNP and Triplet LNP in mice bearing orthotopic E0771 TNBC tumors (Supplementary Fig. 3F, G). In contrast to the MC38 tumor model, the E0771 model was susceptible to 4-1BBL monotherapy as complete tumor regression was observed in 3 out 7 mice (Supplementary Fig. 3G). The combination of IL-7 and IL-21 promoted complete tumor regression in 4 out 7 E0771 tumor-bearing mice, while the Triplet LNP led to 6 out 7 complete regressors, suggesting that 4-1BBL is essential for the therapeutic efficacy of the Triplet LNP, particularly against E0771 tumors (Supplementary Fig. 3G). Then, we compared the therapeutic efficacy of the Triplet LNP to the ICB anti-PD1 in E0771 tumor-bearing mice (Fig. 2G, H). The Triplet LNP alone was sufficient to induce complete tumor regression in a notable 10 out of 12 E0771 tumor-bearing mice, strongly outperforming anti-PD1 (1 of 12 complete regressors) (Fig. 2H). Remarkably, combining the Triplet LNP treatment with anti-PD1 completely eradicated the E0771 tumors (12 out of 12 complete regressors) (Fig. 2H). Moreover, we investigated the

therapeutic efficacy of the Triplet LNP and anti-PD1 in the subcutaneous B16F10 melanoma model. While both the Triplet LNP and anti-PD1 monotherapy failed to improve survival, the Triplet LNP/anti-PD1 combination significantly enhanced survival with 4 out of 10 complete regressors (Fig. 2I, J), showcasing the synergistic potential of the Triplet LNP and anti-PD1 in non-responsive models.

Triplet LNP displays a favorable safety profile
Considering the established dose-limiting hepatotoxicity of 4-1BB agonists[29–32], we sought to assess the potential hepatotoxicity of the Triplet LNP treatment. Generally, all treated mice tolerated the therapy well, experienced no weight loss, and showed no signs of acute toxicity. Serum alanine transaminase (ALT) and aspartate transaminase (AST) activities measured 4 and 24 h after the first injection and as well as four days following the third injection were not elevated in Triplet LNP-treated mice (Supplementary Fig. 4A–E). Flow cytometry analysis of the livers four days following the third dose revealed a slight increase in the frequency of CD45$^+$ cells in the Triplet LNP-treated mice, but no significant impact on the frequencies of monocytes or T cells, including CD4$^+$ T cells and CD8$^+$ T cells (Supplementary Fig. 4F–K). Additionally, we performed hematoxylin and eosin (H&E) and Sirius Red stainings to assess the effects of the Triplet LNPs on the microanatomy of the liver four days and eight weeks (complete regressors) following the third injection (Supplementary Fig. 5). Compared to vehicle-treated mice, a slight increase in lobular inflammation was seen in LNP-treated mice four days after the third dose, which tended to be more elevated in the Triplet LNP-treated group (Supplementary Fig. 5A and Supplementary Table 1). No increase in portal or biliary inflammation was observed at this timepoint (Supplementary Fig. 5A and Supplementary Table 1). The Triplet LNP treatment also resulted in a slightly elevated fibrosis score. Nonetheless, eight weeks after the third dose, Triplet LNP-treated complete regressors did not show signs of increased liver inflammation or fibrosis in comparison to vehicle-treated mice (Supplementary Fig. 5A, B and Supplementary Table 1). Overall, these data indicate that intratumoral administration of the Triplet LNP is well tolerated and does not elicit profound or long-lasting hepatoxicity, in sharp contrast to what has been reported for systemic treatment with 4-1BB agonistic antibodies[40].

Triplet LNP eradicates tumors by promoting CD8$^+$ T-cell infiltration and activation
We investigated the impact of the Triplet LNP on the immune effector cells within the tumor two days following the second intratumoral injection (Fig. 3A, B and Supplementary Fig. 6A). The Triplet LNP tremendously increased the frequency of CD8$^+$ T cells and consequently, the frequency of TAMs decreased, though the relative frequency of CD11c^{hi} MHC-II$^+$ TAMs remained constant across the different treatments (Fig. 3C, D and Supplementary Fig. 6B). Despite the increase in the frequency of CD8$^+$ T cells, the Triplet LNP did not improve their proliferative capacity, however, it increased the proportion of CD44^{hi}
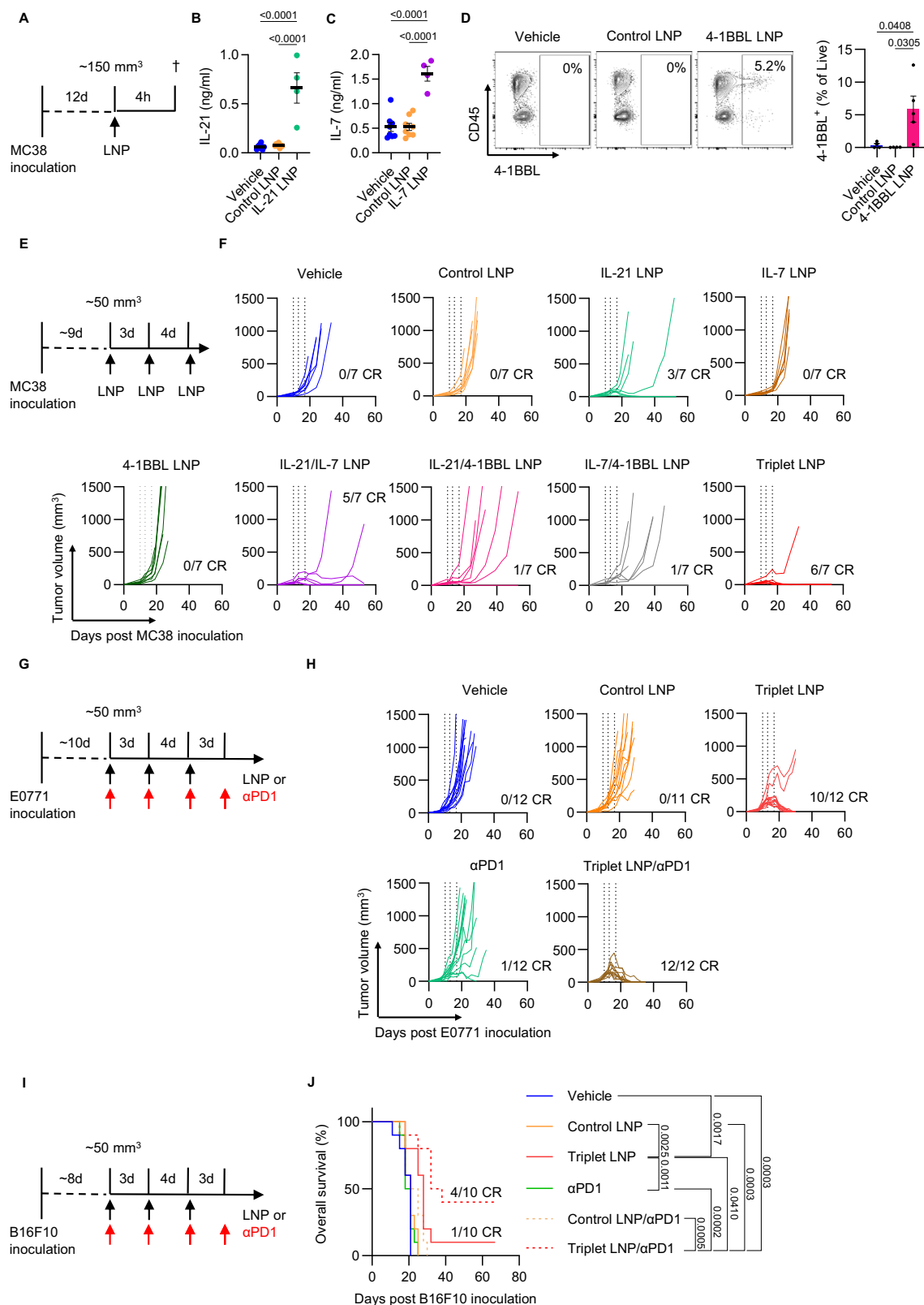
CD62L^{lo} effector CD8^{+} T cells (Fig. 3E and Supplementary Fig. 6C). Moreover, the Triplet LNP significantly induced cytotoxic granzyme B^{+} CD8^{+} T cells and enhanced the capacity of CD8^{+} T cells to produce IFN-γ and TNF-α (Fig. 3F, G). Although the Triplet LNP had no impact on the abundance of NK cells in the tumor, the frequency of granzyme B[+] and IFN-γ[+] TNF-α^{+} NK cells increased significantly in the tumor (Fig. 3H–J). To dissect the role of the separate components of the Triplet LNP, the

changes within the TME were assessed two days following the second intratumoral injection of either IL-21 LNP, IL-21/IL-7 LNP, IL-21/4-1BBL LNP, or Triplet LNP (Fig. 3A). While IL-21 was sufficient to increase the frequency of granzyme B^{+} CD8^{+} T cells in the tumor, only the combination of IL-21 with IL-7 improved CD8^{+} T-cell infiltration into the tumor two days following the second intratumoral injection (Supplementary Fig. 6D, E). Interestingly, the presence of 4-1BBL was necessary

Fig. 2 | Triplet LNP eradicates tumors across multiple preclinical models.
A Schematic outline of experimental procedures. Scatter plots show the concentration of (**B**) IL-21 and (**C**) IL-7 in MC38 tumor supernatants 4 h post intratumoral injection of vehicle ($n = 8$ animals), control LNP ($n = 8$ animals), or cytokine LNP ($n = 4$ animals). **D** Representative flow cytometry plots and bar graph show the frequency of live 4-1BBL$^+$ cells in subcutaneous MC38 tumor 24 h post intratumoral injection of vehicle ($n = 4$ animals), control LNP ($n = 4$ animals), or 4-1BBL LNP ($n = 5$ animals). **E** Schematic outline of experimental procedures. **F** MC38 tumor individual growth curves of mice treated with vehicle, control LNP, IL-21 LNP, IL-7 LNP, 4-1BBL LNP, IL-21/IL-7 LNP, IL-21/4-1BBL LNP, IL-7/4-1BBL LNP and Triplet LNP ($n = 7$ animals/group). Vertical dotted lines indicate intratumoral injections. **G** Schematic outline of experimental procedures. **H** E0771 tumor individual growth curves of

mice treated with vehicle ($n = 12$ animals), control LNP ($n = 11$ animals), Triplet LNP ($n = 12$ animals), anti-PD1 ($n = 12$ animals) and Triplet LNP/anti-PD1 ($n = 12$ animals). Vertical dotted lines indicate intratumoral injections. **I** Schematic outline of experimental procedures. **J** Survival curve of subcutaneous B16F10 tumor-bearing mice treated with vehicle, isotype control, control LNP/isotype control, Triplet LNP/isotype control, anti-PD1, control LNP/anti-PD1, and Triplet LNP/anti-PD1 ($n = 10$ animals/group). **B–D** One-way ANOVA followed by post hoc Tukey's multiple comparisons test and (**J**) log-rank (Mantel-Cox) test were performed. Data shown in (**H**) is pooled from two independent experiments. Bars and horizontal lines show mean. Error bars indicate SEM. Source data are provided as a Source Data file. CR, complete regressor; SEM, standard error of mean.

---

to maintain the levels of CD11c^{hi} MHC-II$^+$ pro-inflammatory TAMs in the tumor (Supplementary Fig. 6F).

Next, we evaluated the impact of the Triplet LNP on the immune landscape of the E0771 tumors two days following the second intratumoral injection (Supplementary Fig. 6G). The Triplet LNP treatment enhanced CD8$^+$ T-cell infiltration in the tumor, which was accompanied by a shift toward an activated effector memory state and a higher production of granzyme B, IFN-γ, and TNF-α (Supplementary Fig. 6H–L). Moreover, the Triplet LNP reduced the frequency of TAMs, with no significant changes in the frequency of MHC-II$^+$ TAMs (Supplementary Fig. 6M, N).

The observed increase in the frequency of CD8$^+$ T cells in the Triplet LNP-treated MC38 tumor-bearing mice was not restricted to the TME. In the blood of the Triplet LNP-treated mice, a consistent increase in the frequency of T cells, in particular CD8$^+$ T cells, was observed as of five days post the first intratumoral injection (Supplementary Fig. 7A). It has been shown that the frequency of the CX3CR1$^+$ subset of circulating CD8$^+$ T cells correlates with response to immune checkpoint blockers and survival of MC38 tumor-bearing mice and non-small cell lung carcinoma (NSCLC) patients, hence it can be used as a blood-based biomarker of response to immunotherapy[41,42]. Interestingly, the frequency of tumor-matching CD8$^+$ T cells within the CD8$^+$ T-cell population in the blood, identified here as CD39$^+$ CX3CR1$^+$ CD8$^+$ T cells, increased significantly in the Triplet LNP-treated mice in comparison to the control cohorts (Fig. 3K). Hence, the presence of CD39$^+$ CX3CR1$^+$ CD8$^+$ T cells in the blood could potentially be used as a prognostic marker for the response to Triplet LNP therapy. Accordingly, the frequency of CD4$^+$ T cells in the Triplet LNP-treated mice slightly decreased over time compared to the control cohorts (Supplementary Fig. 7B). Next, we sought to determine whether NK cells or CD8$^+$ T cells are required for the therapeutic efficacy of the Triplet LNP. Using anti-NK1.1 and anti-CD8-depleting antibodies, we found that while the partial depletion of NK cells did not affect the therapeutic efficacy of the Triplet LNP, the depletion of CD8$^+$ T cells abolished the therapeutic effect completely, indicating that the therapeutic efficacy of the Triplet LNP is CD8$^+$ T cell-dependent (Fig. 3L, M and Supplementary Fig. 7C, D).

Triplet LNP alters the relative abundance of CD8$^+$ T-cell subsets within the TME
To decipher the impact of the Triplet LNP on the different CD8$^+$ T-cell subsets in the TME, we performed CITE-seq on the immune-cell compartment of the tumor. In line with our flow cytometry results, the T-cell compartment increased profoundly in tumors of the Triplet LNP-treated mice compared to vehicle and control LNP-treated mice (Fig. 4A and Supplementary Fig. 8A, B). High-resolution subclustering of the T-cell compartment based on the transcriptome and selected surface proteins revealed twelve distinct clusters of which the proportions of CD8T Prf1 Lag3 hi, CD8T Ccl3 Nr4a3 and CD8T Ccr2 Gzma clusters increased in the tumors of the Triplet LNP-treated mice (Fig. 4B and Supplementary Fig. 8C, D). In the CD8T Prf1 Lag3 hi cluster, which showed an 8-fold increase upon treatment with the

Triplet LNP, genes associated with T-cell exhaustion (*Entpd1*, *Lag3*, *Pdcd1*, *Havcr2*) and effector function (*Prf1*, *Gzmf*, *Gzmc*, *Ccl3*, *Ccl4*) were upregulated (Fig. 4C and Supplementary Fig. 8E). Accordingly, the expression of the respective T-cell exhaustion proteins (CD39, CD223 (LAG3), PD1, CD366 (TIM-3)) strongly correlated with that of the genes (Fig. 4D and Supplementary Fig. 9A). Gene ontology (GO) enrichment analysis of the upregulated genes in this CD8T Prf1 Lag3 hi cluster showed enrichment in GO terms associated with the regulation of T-cell activation and cytotoxicity (Fig. 4E). In the CD8T Ccl3 Nr4a3 cluster, genes of several proinflammatory cytokines and chemokines (*Tnf*, *Ifng*, *Ccl3*, *Ccl4*, *Xcl1*) were upregulated, suggesting their potential role in attracting and activating other immune cells including T cells, NK cells and DCs (Fig. 4C). The CD8T Ccr2 Gzma cluster exhibited a limited set of differentially upregulated genes, which included *Ccr2*, *Gzma*, and *Ccl5* (Fig. 4C). To identify the phenotypic state of these clusters, we projected our T-cell cluster onto the tumor-infiltrating T-cell atlas by Andreatta et al.[43], which identified CD8T Prf1 Lag3 hi, CD8T Ccl3 Nr4a3 and CD8T Ccr2 Gzma as exhausted, progenitor exhausted and effector memory, respectively (Supplementary Fig. 9B). Despite having a tremendous impact on the abundance of different CD8$^+$ T-cell states in the tumor, the Triplet LNP treatment had a minimal impact on the overall cytotoxic and exhaustion signatures within these subsets (Fig. 4F).

Triplet LNP improves myeloid-CD8$^+$ T-cell interactions
To identify the cellular targets of the Triplet LNP treatment, we assessed the expression levels of *Il21r*, *Il7r*, and *Tnfrsf9* (encoding 4-1BB receptor) across the different immune cell subsets in the tumor. *Il21r* transcripts were expressed at varying levels in B cells, T cells, DCs, TAMs, and monocytes, while the expression of *Il7r* and *Tnfrsf9* was restricted mostly to DCs and lymphocytes (Supplementary Fig. 9A). Therefore, we speculated that the Triplet LNP treatment might have direct and indirect effects on the abundance and activation of different myeloid cell subsets. We subclustered the DC compartment into five clusters in which the migDC cluster was slightly more abundant in the Triplet LNP-treated mice (Fig. 5A and Supplementary Fig. 10B, C). Additionally, the Triplet LNP increased the expression of genes associated with DC maturation in the cDC1 and cDC2 clusters without altering genes associated with DC regulation/exhaustion (Fig. 5B–D). It has been recently shown that successful immunotherapy led to the transient increase and expansion of a distinct neutrophil subset with an IFN-stimulated gene signature[44]. In line with these findings, we observed an expansion in two neutrophil clusters with IFN-stimulated gene signatures upon the Triplet LNP treatment, namely Cxcl2hi Gbp4hi and Cxcl2hi IFN neutrophils (Fig. 5E). The TAM/Monocyte compartment was clustered into six subclusters based on the transcriptome and surface protein markers in which the relative abundance of the Mac immature cluster increased upon the Triplet LNP treatment (Supplementary Fig. 10D–F). Accordingly, the proportion of the Mac hypoxic and Mac prolif decreased (Supplementary Fig. 10D). Here, the Triplet LNP treatment elevated the transcripts of genes associated with an M1-like phenotype in the Mac immature, Mac
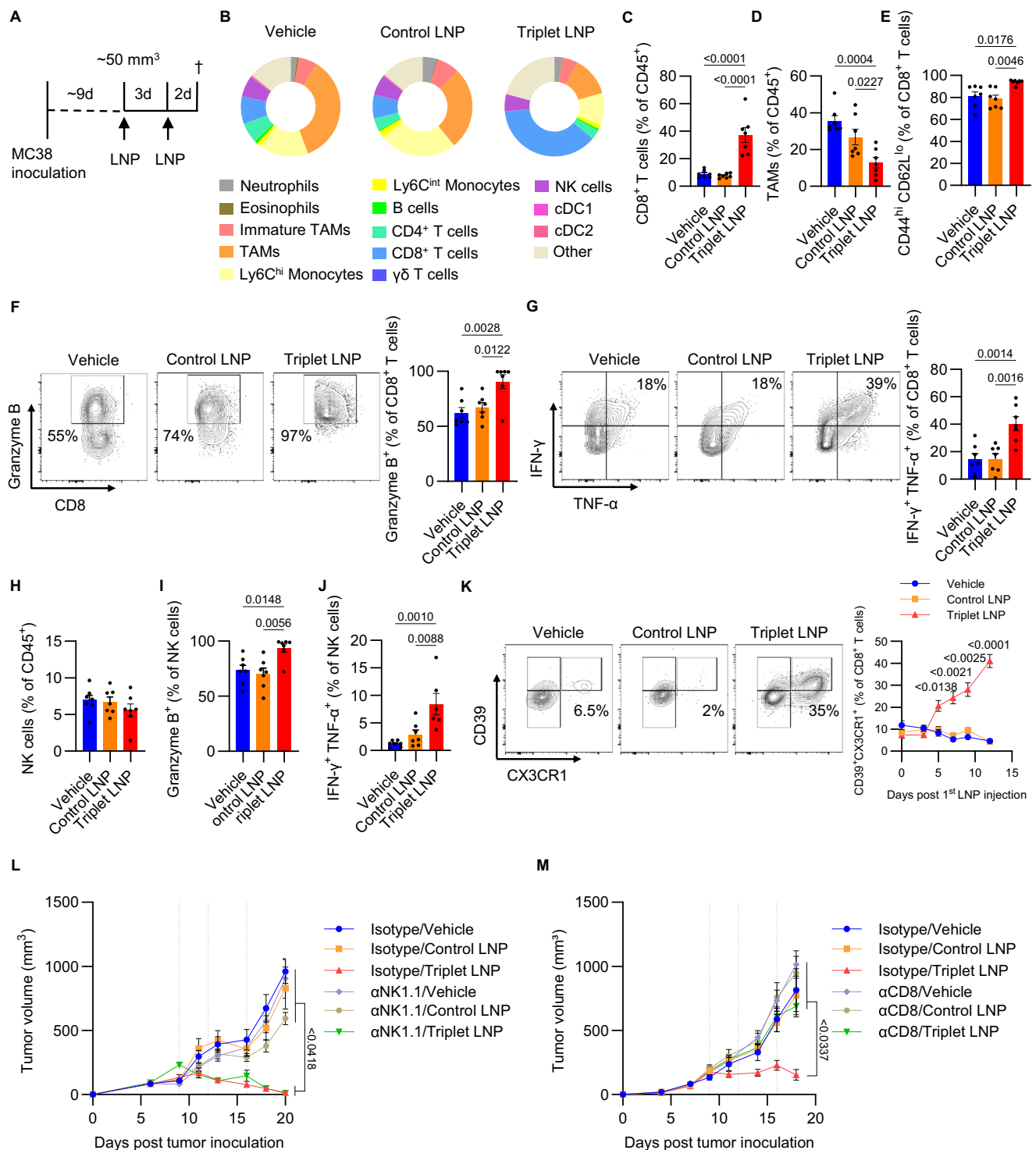
Fig. 3 | Triplet LNP promotes intratumoral CD8+ T-cell infiltration and activation. A Schematic outline of experimental procedures. **B** Pie charts show the mean frequency of immune subsets within CD45+ cells in the tumor of vehicle-, control LNP- or Triplet LNP-treated mice quantified using flow cytometry (*n* = 7 animals/group). Bar graphs show the frequency of (**C**) CD8+ T cells, (**D**) TAMs, (**E**) CD44hi CD62Llo CD8+ T cells, (**F**) Granzyme B+ CD8+ T cells, (**G**) IFN-γ+ TNF-α+ CD8+ T cells, (**H**) NK cells (**I**) Granzyme B+ NK cells within MC38 tumors treated with vehicle, control LNP or Triplet LNP (*n* = 7 animals/group) and (**J**) IFN-γ+ TNF-α+ NK cells within MC38 tumors treated with vehicle (*n* = 7 animals), control LNP (*n* = 7 animals) or Triplet LNP (*n* = 6 animals). **K** Representative flow cytometry plots and graph show the frequency of CD39+ CX3CR1+ CD8+ T cells over time in the blood of vehicle (*n* = 5 animals), control LNP (*n* = 5 animals), and Triplet LNP-treated mice (*n* = 6 animals). MC38 tumor growth curves upon (**L**) isotype or αNK1.1 administration

(isotype/vehicle *n* = 5 animals; isotype/control LNP *n* = 5 animals; isotype/triplet LNP *n* = 6 animals; αNK1.1/vehicle *n* = 5 animals; αNK1.1/control LNP *n* = 5 animals; αNK1.1/triplet LNP *n* = 6 animals) and (**M**) isotype or αCD8 administration (isotype/vehicle *n* = 9 animals; isotype/control LNP *n* = 9 animals; isotype/triplet LNP *n* = 12 animals; αCD8/vehicle *n* = 10 animals; αCD8/control LNP *n* = 10 animals; αCD8/triplet LNP *n* = 12 animals). **C**–**J** One-way ANOVA followed by post hoc Tukey's multiple comparisons test and (**K**–**M**) repeated measures two-way ANOVA followed by post hoc Tukey's multiple comparisons test were performed. Data shown in (**B**–**J**) are representative of three independent experiments. Data shown in (**K**) is representative of two independent experiments. Data shown in (**M**) is pooled from two independent experiments. Bars and horizontal lines show mean. Error bars indicate SEM. Source data are provided as a Source Data file. SEM, standard error of mean; TAMs, tumor-associated macrophages.
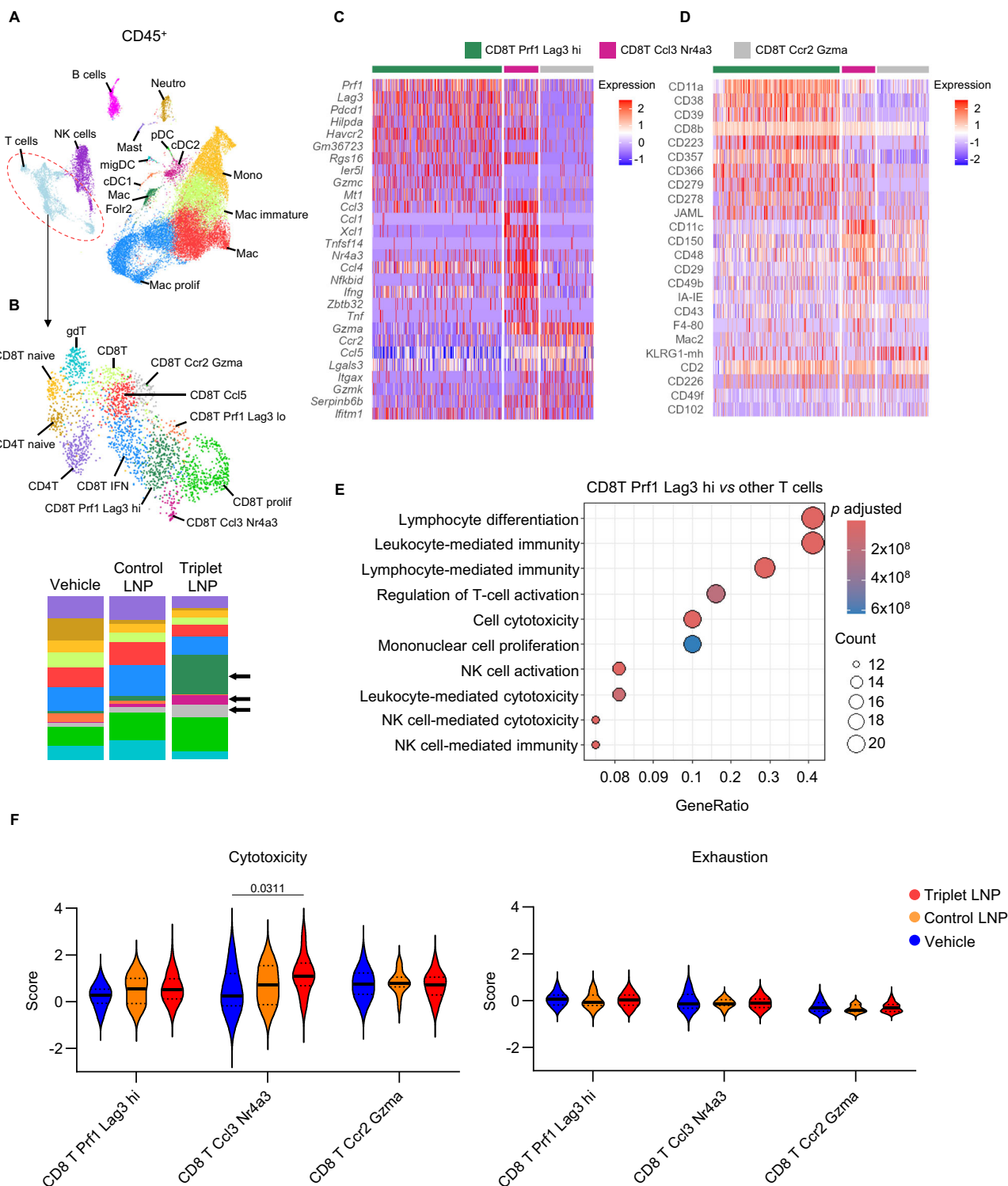
Fig. 4 | Triplet LNP alters the relative abundance of CD8+ T-cell subsets within the TME. A UMAP plot of CITE-seq dataset containing 30208 CD45+ sorted cells from MC38 tumors of vehicle, control LNP, and Triplet LNP-treated mice (*n* = 5 animals/group). **B** High-resolution subclustering of the T-cell compartment of the dataset is shown. Bars show the frequency of different T-cell subsets in the tumor dataset across different treatments. **C** Heatmap of the top 10 differentially expressed genes in the CD8T Prf1 Lag3 hi, CD8T Ccl3 Nr4a3 and CD8T Ccr2 Gzma clusters. **D** Heatmap of the top 10 differentially expressed proteins in the CD8T Prf1 Lag3 hi, CD8T Ccl3 Nr4a3 and CD8T Ccr2 Gzma clusters. **E** GO term enrichment analysis of the differentially upregulated genes in the CD8T Prf1 Lag3 hi cluster in comparison to all other T-cell clusters in the tumor dataset. **F** Violin plots show combined mean expression values for the indicated genes (score) for the cytotoxic T cell markers (*Gzma, Gzmb, Prf1, Tnf, Ifng, Cxcr6*) or exhaustion markers (*Pdcd1, Ctla4, Tigit, Lag3, Havcr1, Tox, Nrp1*) in cells of the CD8T Prf1 Lag3 hi, CD8T Ccl3 Nr4a3 and CD8T Ccr2 Gzma clusters in vehicle-, control LNP- and Triplet LNP-treated mice. One-way ANOVA followed by post hoc Tukey's multiple comparisons test was performed. Source data for (**F**) are provided as a Source Data file. GO, gene ontology; UMAP, uniform manifold approximation and projection.
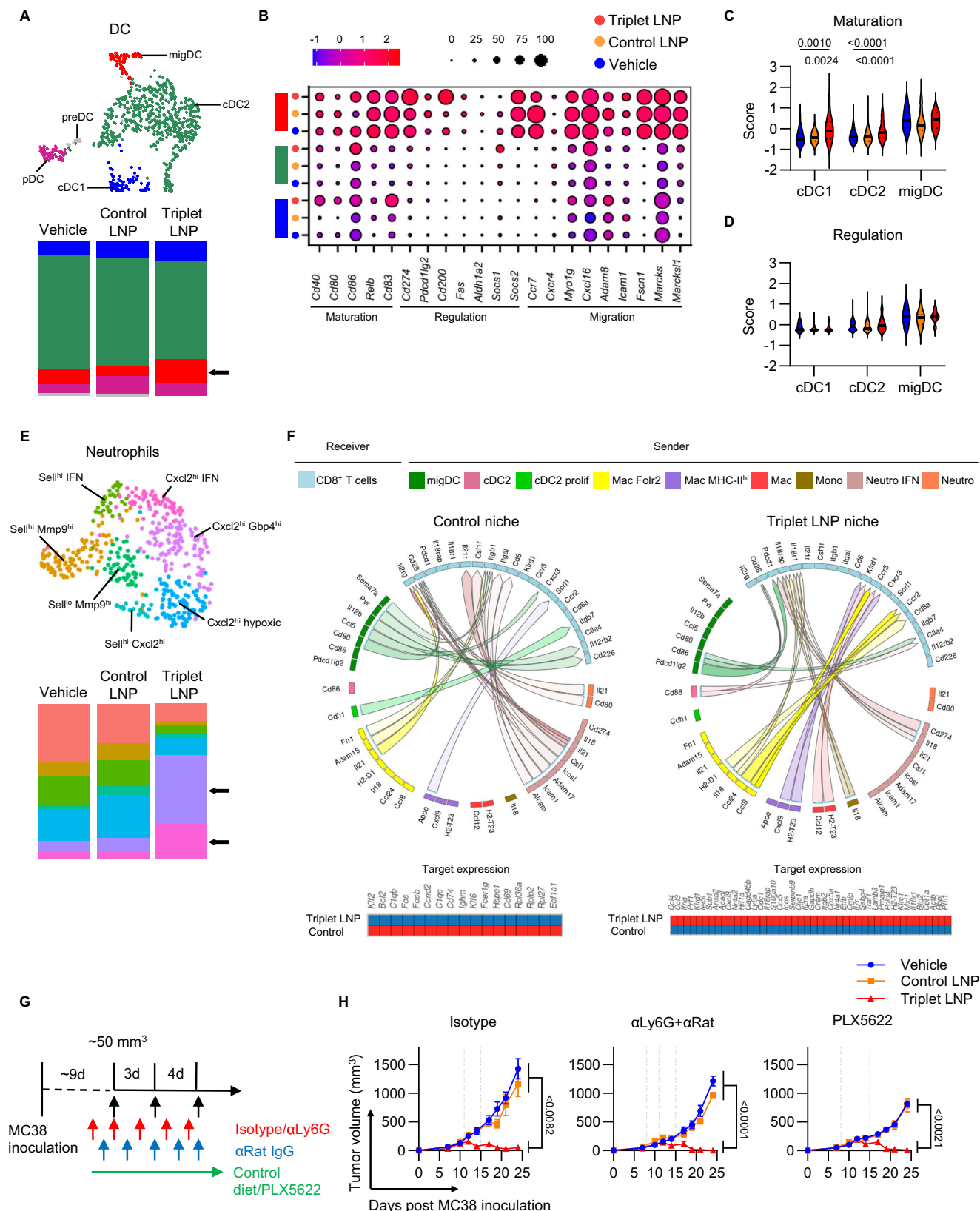
MHCII-hi, Mac hypoxic and Mac prolif clusters (Supplementary Fig. 10G, H). Altogether, our data indicate that the Triplet LNP treatment led to notable changes in the myeloid compartment in terms of both the abundance of distinct subsets and their gene expression profile. Next, to determine the effect of the treatment on the myeloid-CD8+ T-cell interactions, we performed a differential Nichenet analysis

to predict the niche-specific ligand-receptor pairs between the different myeloid cell subsets and CD8+ T cells in the control niche (vehicle + control LNP) and Triplet LNP niche. The differential Nichenet approach predicts ligand-receptor pairs that are both differentially expressed and show enrichment of the expression of their known target genes between conditions. From the top 50 ligand-receptor interactions in

Fig. 5 | Triplet LNP improves myeloid-CD8+ T-cell interactions. A UMAP plot shows high-resolution clustering of the DC compartment in the CITE-seq dataset of the tumor. Bars show the frequency of different DC subsets in the tumor dataset across different treatments. **B** Dot plot highlights differentially expressed genes associated with maturation, regulation, and migration in distinct DC clusters of the tumor CITE-seq dataset across different treatments. Dot size represents the percentage of cells expressing the gene and color gradient represents average scaled expression within a cell cluster. Violin plots show combined mean expression values for the indicated genes (score) for (**C**) maturation markers (*Cd40, Cd80, Cd86, Relb, Cd83*) and (**D**) regulation (*Axl, Ccl19, Ccl22, Aldh1a1*) in cells of the DC clusters in vehicle-, control LNP- and Triplet LNP-treated mice. One-way ANOVA followed by post hoc Tukey's multiple comparisons test was performed. **E** UMAP plot shows high-resolution clustering of the neutrophil compartment in the tumor CITE-seq dataset. Bars show the relative abundance of the different neutrophil subsets in the tumor CITE-seq dataset across different treatments. **F** Circle plot shows links between top predicted ligands for migDC, cDC2, cDC2 prolif, Mac Folr2, Mac MHC-II-hi, Mac, Mono, Neutro IFN, and the Neutro clusters and their associated receptors found on CD8+ T cells within the control niche and Triplet LNP niche of the tumor CITE-seq dataset. The transparency of the linking arrow reflects the prioritization score of the ligand-receptor pair. The heatmaps below show the scaled average expression level of the top target genes that are potentially regulated by the predicted ligand-receptor pairs. **G** Schematic outline of experimental procedures. **H** MC38 tumor growth curves upon isotype/control diet or αLy6G or PLX5622 diet administration (*n* = 6 animals/group). Repeated measures two-way ANOVA followed by post hoc Tukey's multiple comparisons test were performed. Error bars indicate SEM. Source data for (**C, D, H**) are provided as a Source Data file. CITE, cellular indexing of transcriptomes and epitopes by sequencing; SEM, standard error of mean; UMAP, uniform manifold approximation and projection.

the Triplet LNP niche, the most numerous links were found with ligands specific for the Mac Folr2, migDC and Neutro IFN clusters (Fig. 5F). Among the top differentially expressed ligands in the Triplet LNP niche were the migDC-specific co-stimulatory molecule *Cd86* and the proinflammatory cytokines *Il18* (enriched in Mono and Mac Folr2) and *Cxcl9* (upregulated in Mac MHCII-hi) (Fig. 5F). The predicted target genes of the top Triplet LNP-specific ligand-receptor pairs included *Ccl4, Ccl3, Ifng, Prf1, Cxcl9, Nr4a1, Nr4a2,* and *Il2ra*, which are associated with CD8+ T-cell effector functions and activation (Fig. 5F). These results suggest that upon Triplet LNP therapy, distinct myeloid populations contribute to the activation of cytotoxic CD8+ T cells in the TME. Nevertheless, the depletion of neutrophils or TAMs using anti-Ly6G/anti-rat antibodies or the CSF1R inhibitor PLX5622, respectively, had no impact on the therapeutic efficacy of the Triplet LNP (Fig. 5G, H and Supplementary Fig. 11A, B).
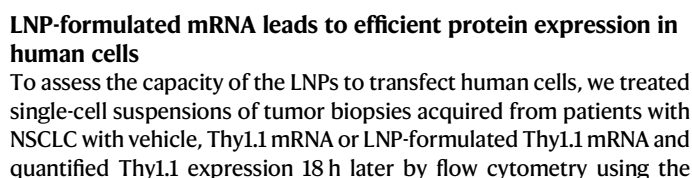
Triplet LNP enhances CD8+ T-cell activation and proliferation in the tdLN

In contrast to the TME, within the tdLN of MC38 tumor-bearing mice, the Triplet LNP treatment had a less profound effect on the relative abundance of the immune cell populations two days after the second intratumoral injection (Fig. 3A). We observed a slight increase in B cell frequency, accompanied by a decrease in the frequency of CD4+ T cells, including FoxP3+ Tregs (Fig. 6A and Supplementary Fig. 12A–C). While the Triplet LNP had no impact on the frequency of CD8+ T cells in the tdLN, it induced CD8+ T-cell proliferation and enhanced their cytotoxic capacity and their differentiation toward a central memory phenotype (Fig. 6B–D and Supplementary Fig. 12D). Of note, CD8+ T-cell activation was also observed in the tdLN of Triplet LNP-treated E0771 tumor-bearing mice (Supplementary Fig. 12E, F). Next, we performed CITE-seq on CD45+ cells of tdLN of vehicle-, control LNP- and Triplet LNP-treated mice (Fig. 6E). High-resolution multimodal clustering of the T/NK-cell compartment revealed thirteen distinct clusters, of which the abundance of CD8T Ctla2a Ifng, CD8T Ctla2a and CD8T prolif clusters was slightly increased in the tdLN of the Triplet LNP-treated mice (Fig. 6E and Supplementary Fig. 12G). The Triplet LNP treatment induced the expression of various effector genes in the CD8T Ctla2a Ifng cluster, including *Prf1, Ifng, Gzma, Gzmb, Fasl,* and *Tnf*. Interestingly, it also induced the expression of the chemokine receptor *Cxcr6*, which has been reported to play a crucial role in the optimal positioning of CD8+ T cells to interact with activated DCs within the TME[45] (Fig. 6F). Since our data suggests that LNP uptake might promote cDC2 activation and migration toward the tdLN (Fig. 1E–G), we sought to determine the effect of the Triplet LNP treatment on DC-CD8+ T-cell interactions in the tdLN. For this, we performed a differential Nichenet analysis to predict niche-specific ligand-receptor pairs between different cDC subsets and CD8+ T cells in the control niche (Vehicle + Control LNP) and the Triplet LNP niche (Supplementary Fig. 12H, I). The analysis predicted different interactions in the Triplet LNP niche, in particular, Triplet LNP induced migDC-CD8+ T-cell and cDC2-CD8+ T-cell interaction pairs in which *Cd80, Cd86, Cxcl16,* and *Cxcl10* were among the top differentially expressed ligands (Supplementary Fig. 12I). The target genes of these ligand-receptor interactions were mapped, highlighting the upregulated expression of genes associated with CD8+ T-cell effector function and proliferation in the Triplet LNP niche, including *Ccl4, Ccl5, Gzma, Ifng,* and *Mki67* (Supplementary Fig. 12I). Hence, this data suggests that upon Triplet LNP treatment, cDC2s and migDCs induce cytotoxic CD8+ T cells in the tdLNs. To investigate whether the trafficking of the CD8+ T cells from the tdLN to the tumor is necessary for the therapeutic efficacy of the Triplet LNP, we blocked T-cell egression using the S1PR inhibitor FTY720 (Supplementary Fig. 12J). FTY720 treatment diminished the therapeutic efficacy of the Triplet LNP (5 of 11 complete regressors), indicating that CD8+ T-cell trafficking is necessary for optimal therapeutic efficacy (Fig. 6G). Given that Triplet LNP therapy induces central memory CD8+ T cells in the tdLN, we investigated whether the Triplet LNP treatment conferred systemic long-term immunity. Indeed, we found that splenic CD8+ T cells from Triplet LNP-treated mice secreted higher levels of IFN-γ in response to the p15E peptide, an immunodominant MHC-I-restricted epitope of MC38 (Fig. 6H). More importantly, Triplet LNP-treated complete regressors remained immune to MC38 and E0771 cancer cells when rechallenged sixty days after initial tumor inoculation (Fig. 6I).

Intratumoral injection of Triplet LNP induces regression of distal tumors

Having demonstrated that the Triplet LNP treatment led to CD8+ T-cell activation in the tdLN, conferred long-term immunity and significantly increased the frequency of tumor-matching CD39+ CX3CR1+ CD8+ T cells in the blood, we aimed at evaluating the abscopal effects of the Triplet LNP treatment. Hereto, mice were inoculated with MC38 tumors at two different subcutaneous sites (left and right flanks), but only the tumor on the right flank was treated with vehicle, control LNP or Triplet LNP (Fig. 7A). While the Triplet LNP-treated tumors all completely regressed, interestingly, the treatment significantly reduced the growth of the distal non-treated tumor, improving the overall survival (Fig. 7B–D). Similarly, in the less immunogenic E0771 model (Fig. 7E), the Triplet LNP therapy also reduced local and distal tumor growth, prolonging overall survival (Fig. 7F–H). In addition, we utilized a pseudometastasis approach in which mice were inoculated with E0771 cancer cells in the mammary fat pad before they received an intravenous injection of E0771 cancer cells a day later to induce lung metastasis (Supplementary Fig. 13A). Local injection of the Triplet LNP reduced lung tumor burden and improved overall survival, leading to 2 out of 6 complete regressors (Supplementary Fig. 13B–D).

LNP-formulated mRNA leads to efficient protein expression in human cells

To assess the capacity of the LNPs to transfect human cells, we treated single-cell suspensions of tumor biopsies acquired from patients with NSCLC with vehicle, Thy1.1 mRNA or LNP-formulated Thy1.1 mRNA and quantified Thy1.1 expression 18 h later by flow cytometry using the gating strategies depicted in Supplementary Fig. 14A, B. Thy1.1 LNPs resulted in improved expression compared to naked Thy1.1 mRNA (Fig. 8A). The Thy1.1 LNP transfected both the CD45+ immune cells and CD45- non-immune cells (Fig. 8B). Within the CD45+ compartment, Thy1.1 expression was most pronounced in myeloid cells, in particular, macrophages (Fig. 8C–E). This data indicates that the LNPs can

Fig. 6 | Triplet LNP enhances CD8⁺ T-cell activation and proliferation in the tdLN and induces immunological memory. A Pie charts show the mean frequency of immune subsets within CD45⁺ cells in the tdLN quantified by flow cytometry (*n* = 7 animals/group). Bar graphs show the frequency of (**B**) Ki-67⁺ CD8⁺ T cells, (**C**) Granzyme B⁺ CD8⁺ T cells and (**D**) CD44ʰⁱ CD62Lʰⁱ CD8⁺ T cells in the tdLN (*n* = 7 animals/group). **E** UMAP plot of CITE-seq dataset containing CD45⁺ sorted cells from tdLN of vehicle, control LNP, and Triplet LNP-treated mice (*n* = 5 animals/group). High-resolution clustering of the T-cell compartment of the dataset is shown on the right. Below, pie charts show the relative abundance of different T-cell subsets in the tdLN dataset across different treatments. **F** Dot plot highlights differentially expressed genes associated with effector function and migration in distinct CD8⁺ T-cell clusters of the tdLN CITE-seq dataset across different treatments. Dot size represents the percentage of cells expressing the gene and color gradient represents average scaled expression within a cell cluster. **G** Schematic outline of experimental procedures and survival curves of MC38 tumor-bearing mice treated with vehicle, control LNP or Triplet LNP in the presence or absence of

FTY720 (0.9% NaCl/vehicle *n* = 12 animals; 0.9% NaCl/control LNP *n* = 10 animals; 0.9% NaCl/triplet LNP *n* = 11 animals; FTY720/vehicle *n* = 11 animals; FTY720/control LNP *n* = 12 animals; FTY720/triplet LNP *n* = 11 animals). **H** Bar graph shows the IFN-γ-secreting CD8⁺ T cells from spleens of naïve mice (*n* = 8 animals), vehicle-treated mice (*n* = 7 animals), control LNP-treated mice (*n* = 6 animals), and Triplet LNP-treated mice (*n* = 8 animals). **I** Schematic outline of experimental procedures and MC38 (control *n* = 17 animals; rechallenge=8 animals) and E0771 (control *n* = 4 animals; rechallenge *n* = 6 animals) tumor growth curves of control mice and rechallenged complete regressors. **B–D**, **H** One-way ANOVA followed by post hoc Tukey's multiple comparisons test and (**G**) Gehan-Breslow-Wilcoxon test were performed. Data shown in (**A–D**) are representative of three independent experiments. Data shown in (**G**) is pooled from two independent experiments. Bars show mean. Error bars indicate SEM. Source data for (**A–D**, **G–I**) are provided as a Source Data file. CITE, cellular indexing of transcriptomes and epitopes by sequencing; FTY720, fingolimod; tdLN, tumor-draining lymph node; SEM, standard error of mean; UMAP, uniform manifold approximation and projection.

---

efficiently transfect immune and non-immune human cells with a noticeable bias toward myeloid cells. Finally, we sought to corelate the expression of *IL21*, *IL7*, and *TNFSF9* with the overall survival of patients with cancer that were not treated with immunotherapy, including 9 tumor types, using the KM plotter[46]. This analysis demonstrates that higher expression of *IL21*, *IL7*, *TNFSF9*, and their combination are associated with better overall survival with the expression of the combination showing the most significant correlation with better overall survival (Fig. 8F), suggesting that the Triplet LNP might potentially improve the survival of patients with cancer.

Discussion

Intratumoral administration of mRNA encoding immunomodulatory proteins, such as cytokines and costimulatory molecules, holds tremendous potential as an immunotherapeutic platform due to its high potency, safety, and versatility. Local delivery of a saline-formulated Thy1.1-encoding mRNA showed a relatively poor translation efficiency within immune and non-immune cells in the TME, which would necessitate high dosage and administration frequency to achieve therapeutic efficacy[4]. In this study, we developed LNPs using the ionizable cationic lipid S-Ac7-DOG, which was previously shown to be a low inflammatory LNP with a distinct biodistribution compared to the approved MC-3 LNP (Onpattro™) formulation upon intramuscular injection, with improved local mRNA expression, yet strongly reduced off-target expression in liver[33]. We demonstrate that LNP-formulated Thy1.1 mRNA enabled higher expression levels of Thy1.1 compared to naked Thy1.1 mRNA in immune and non-immune cells within the tumor. Within the immune cells, the Thy1.1 expression was restricted to the myeloid compartment, particularly TAMs, monocytes, and cDC2s. In line with our findings, LNP-formulated OX40 ligand (OX40L) mRNA was reported to lead to OX40L expression in CD11b⁺ myeloid cells in the tumor, with the three most abundant subsets being TAMs, monocytes, and granulocytes[6]. Our findings show that cDC2s possessed the highest intrinsic expression levels of Thy1.1 following the intratumoral administration of Thy1.1 LNP and Thy1.1⁺ cDC2s expressed higher levels of CD80 and CCR7, which was also observed in other studies where LNPs induced mouse and human DC-activation in vitro[47–49]. DCs play a crucial role in antigen trafficking and activation of antigen-specific CD8⁺ T cells in the tdLN. Therefore, activating DCs, and inducing their migration to the tdLN is an advantage of using LNPs to deliver therapeutic mRNA[50–52]. We demonstrate that LNP leakage to the tdLN and spleen is minimal, reflected by minor Thy1.1 expression in comparison to that observed in the tumor. BLI revealed an accumulation of LNPs in the liver, which was described previously, however, we show in our study that the Triplet LNP displayed a favorable safety profile[35]. Despite its safety and potency, intratumoral injections require tumor lesions to be accessible. In this respect, most lesions can now be accessed through guided imaging techniques such as

ultrasound and computerized tomography (CT)[53]. More importantly, local injection of the Triplet LNP conferred systemic protection and induced tumor regression in distal sites.

Recently, mRNA-based immunotherapy targeting CD8⁺ T cells showed notable success in preclinical tumor models: (i) a saline-formulated mRNA mixture encoding IL-12, granulocyte-macrophage colony-stimulating factor (GM-CSF), IL-15, and IFN-α, (ii) LNP-formulated IL-12, and (iii) LNPs loaded with mRNA mixture encoding IL-23, IL-36γ, and OX40 ligand (OX40L) have all eradicated tumors in multiple preclinical models in a CD8⁺ T cell-dependent manner[4–6]. Here, we formulated LNPs loaded with an mRNA mixture encoding IL-21, IL-7, and 4-1BBL, aimed at targeting CD8⁺ T cells to improve their infiltration and function in the tumor, which is generally associated with better clinical outcomes[54]. IL-21 has been reported to synergize with IL-7 to enhance mouse and human CD8⁺ T-cell expansion and function in vitro[36,38,55]. In agreement with this, we observed that IL-21/IL-7 LNP induced CD8⁺ T-cell expansion and enhanced their capacity to produce granzyme B. IL-21 has been shown to polarize alveolar macrophages toward an M2 phenotype in mice with hypoxia-induced pulmonary hypertension[56]. Similarly, in our tumor model, IL-21 LNP led to a decrease in the frequency of MHC-II⁺ M1-like TAMs in the tumor, which was counteracted in the presence of 4-1BBL. Miki et al. have reported that 4-1BBL signaling regulates macrophage polarization in vitro toward an M1-like phenotype[57]. Since TAMs would take up most of the LNPs and profoundly express 4-1BBL, it is a possibility that this would allow them to maintain an M1-like phenotype in the presence of IL-21 due to 4-1BBL signaling.

The Triplet LNP treatment also enhanced NK-cell capacity to produce granzyme B, IFN-γ, and TNF-α, potentially due to 4-1BBL. Yet, the therapeutic efficacy of the Triplet LNP was CD8⁺ T cell-dependent and NK cell-independent. Transcriptomic analyses revealed a profound impact of the Triplet LNP on the myeloid compartment in the tumor, including the expansion of neutrophil subsets with an IFN-stimulated signature, which has recently been reported to be associated with successful immunotherapy[44]. Moreover, genes associated with M1-like signature were upregulated in several TAM subsets of the Triplet LNP-treated mice. Nevertheless, neutrophil and TAM-depletion did not diminish the therapeutic efficacy of the Triplet LNP, which might be due to the depletion of both pro- and antitumoral subsets. The Triplet LNP treatment also upregulated genes associated with maturation, including *Cd86* and *Cxcl16* in cDC1s and cDC2s. Prokhnevska et al. reported that CD86 is necessary to provide a costimulatory signal to tumor-infiltrating stem-like TCF-1⁺ CD8⁺ T cells to acquire effector functions, while Di Pilato et al. showed that CXCL16 attracts effector CD8⁺ T cells to activated DCs within the tumor to receive a critical survival signal[45,58]. In line with these findings, the Triplet LNP therapy led to an expansion of a CD8⁺ T-cell subset in the tumor that is enriched in genes (*Ifng*, *Tnf*, *Gzma*, *Ccl3*, and *Ccl4*) and GO terms
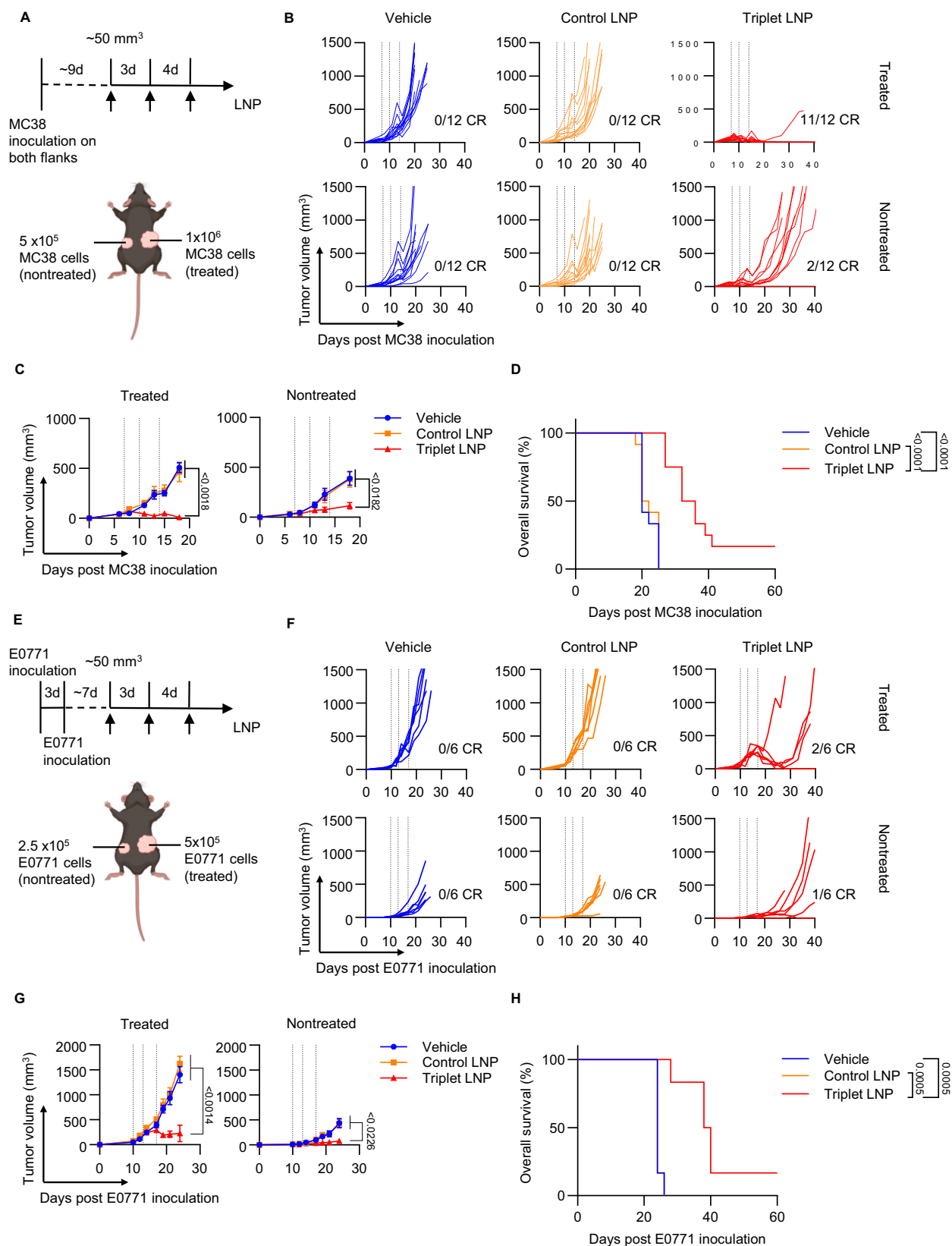
(regulation of T-cell activation and cell cytotoxicity) associated with effector functions.

The tdLN acts as a reservoir of stem-like tumor-specific CD8^{+} T cells that continuously replenish stem-like CD8^{+} T cells in the tumor through continuous migration via the blood[59]. Although Thy1.1 LNP

exhibited limited leakage in the tdLN, our flow cytometry and CITE-seq analyses demonstrated that the Triplet LNP induced CD8^{+} T-cell proliferation and activation in the tdLN. This is potentially due to the enhanced activation and trafficking of cDCs from the tumor to the tdLN upon intratumoral injection of the Triplet LNP. Accordingly, our

Fig. 7 | Intratumoral injection of Triplet LNP induces regression of distal tumors. A Schematic outline of experimental procedures. Created in BioRender. Laoui, D. (2024) https://BioRender.com/j2s690. **B** MC38 tumor individual growth curves of treated and nontreated tumors. Treated (right flank) tumors received three injections of vehicle, control LNP or Triplet LNP ($n = 12$ animals/group). Vertical dotted lines indicate intratumoral injections of the treated tumors. **C** MC38 tumor growth curves of treated and nontreated tumors ($n = 12$ animals/group). Vertical dotted lines indicate intratumoral injections of the treated tumors. **D** Survival curves of MC38 tumor-bearing mice treated with vehicle, control LNP or Triplet LNP ($n = 12$ animal/group). **E** Schematic outline of experimental procedures. Created in BioRender. Laoui, D. (2024) https://BioRender.com/l86l838 **F** E0771

tumor individual growth curves of treated and nontreated tumors. Treated (right flank) tumors received three injections of vehicle, control LNP or Triplet LNP ($n = 6$ animals/group). Vertical dotted lines indicate intratumoral injections of the treated tumors. **G** E0771 tumor growth curves of treated and nontreated tumors ($n = 6$ animals/group). Vertical dotted lines indicate intratumoral injections of the treated tumors. **H** Survival curves of E0771 tumor-bearing mice treated with vehicle, control LNP or Triplet LNP ($n = 6$ animals/group). **C, G** Repeated measures two-way ANOVA followed by post hoc Tukey's multiple comparisons test and (**D, H**) log-rank (Mantel-Cox) test were performed. Horizontal lines show mean. Data shown in (**B–D**) are pooled from two independent experiments. Error bars indicate SEM. Source data are provided as a Source Data file. SEM, standard error of mean.

differential Nichenet analyses predicted stimulatory ligand-receptor pairs between cDC2s and migDCs and CD8^{+} T cells in the Triplet LNP-treated niche. Moreover, we detected a significant increase in the CD39^{+} CX3CR1^{+} tumor-specific CD8^{+} T cells in the blood of the Triplet LNP-treated mice, which were shown to possess higher cytotoxic capacity and be of prognostic relevance[41,42,60]. Ultimately, blocking T-cell trafficking between the tdLN and the tumor using FTY720 diminished the therapeutic efficacy of the Triplet LNP. These results support the hypothesis that cDC2s migrate from the tumor toward tdLN upon Triplet LNP therapy, where they subsequently interact with CD8^{+} T cells, the latter being required for the therapeutic efficacy of Triplet LNP.

In conclusion, we present experimental evidence supporting the potent anti-tumor activity of an mRNA mixture encoding IL-21, IL-7, and 4-1BBL in multiple preclinical tumor models through the development and expansion of tumor-specific effector CD8^{+} T cells. Intratumoral injection of the Triplet LNP conferred long-term protection and showed synergy with the ICB anti-PD1 in ICB-resistant tumor models. Finally, we demonstrate that *IL21*, *IL7*, and *TNFSF9* are predictors of overall survival of patients with cancer.

Methods
Ethical approval
All procedures followed the guidelines of the Belgian Council for Laboratory Animal Science. All experiments were approved by the Ethical Committee for Animal Experiment of the Vrije Universiteit Brussel (Licenses 21-220-14, 21-220-32, 22-220-16, 22-220-18, 22-220-19, 22-220-22, 22-220-23, 22-220-25, 22-220-28, 23-220-11, 24-220-09) and by the Animals Ethics Committee of Ghent University (ECD20/90).

Fresh tumor tissue was obtained from 3 patients with NSCLC undergoing surgical resection at Cliniques Universitaires Saint-Luc-UCLouvain (Brussels, Belgium). The study was approved by the local ethics committees of the Vrije Universiteit Brussel and Saint-Luc-UCLouvain (N° protocole: Immuno Poumon 1) and all patients provided informed consent after the nature and possible consequences of the study had been explained. After resection, samples were immediately transported on ice to the research facilities at Vrije Universiteit Brussel.

mRNA synthesis and purification
All mRNAs were prepared by etherna in vitro transcription (IVT) from etherna plasmids. The final mRNA contains a full replacement of uridine with N1-methyl-pseudouridine. All later experiments were performed using CleanCapped mRNAs. After IVT, double-stranded RNA was removed by cellulose/silica purification. mRNA quality was monitored by capillary gel electrophoresis (Agilent, Belgium). ntrIL21 mRNA was developed by replacing all start codons with stop codons.

Formulation
LNPs were loaded with a mixture of mRNA in a 1:1 ratio. The mRNA was diluted in 100 mM sodium acetate buffer (pH 4), and lipids were dissolved and diluted in ethanol. A nitrogen/phosphate ratio of 10 was

employed for all LNPs. The mRNA and lipid solutions were mixed using a NanoAssemblr Benchtop microfluidic mixing system (Precision Nanosystems) at a flow rate of 9 mL/min and an aqueous/organic phase flow rate ratio of 2:1, followed by dialysis overnight against TBS (20 mM Tris, 0.9% NaCl, pH 7.4). The 4 lipids were prepared at a molar ratio of 50:10:38.5:1.5 (S-Ac7-DOG:DSPC:Cholesterol:DMG-PEG2000). Amicon Ultra Centrifugal Filters (Merck Millipore, 100 kDa molecular weight cutoff) were used for the concentration of LNPs. Size was measured with a Zetasizer Nano (Malvern). mRNA encapsulation efficiency was determined via Quant-iT Ribogreen RNA assay (Thermo Fisher) by comparing lysed LNPs in 1% Triton X-100 (all RNA is detectable) with LNPs in TE buffer (only non-encapsulated RNA is detectable). The assay was performed according to the manufacturer's recommendations.

Animals
Female C57BL/6 J mice aged 6-8 weeks were purchased from Janvier and Charles River. Mice were housed at 20–22 °C, 45–65% humidity with 12 h light/dark cycle. Mice were monitored daily.

Tumor models
MC38 cell line was kindly provided by Massimiliano Mazzone (VIB-KU Leuven, Belgium). E0771 (CRL-3461) and B16F10 (CRL-6475) cell lines were obtained from American Type Culture Collection (ATCC). Cell lines were cultured in Dulbecco's Modified Eagle Medium (DMEM; Gibco) supplemented with 10% (v/v) heat-inactivated fetal calf serum (FCS; Capricorn Scientific), 300 μg/mL L-glutamine, 100 units/mL penicillin, and 100 μg/mL streptomycin. 5×10^5 to 10^6 MC38 and B16F10 cells were injected subcutaneously into the left or right flank of female C57BL/6 mice in 50–200 μL of Hank's Balanced Buffered Saline Solution (HBSS) or Phosphate Buffered Saline (PBS). 5×10^5 E0771 cells were injected orthotopically in the left fourth inguinal mammary fat pad in 50 μL of HBSS. For the MC38 dual-flank tumor model, 1×10^6 cells in 200 μL of HBSS were injected subcutaneously on the right flank and 5×10^5 cells in 200 μL of HBSS were injected on the left flank. For the E0771 dual-mammary fat pad tumor model, 5×10^5 cells in 50 μL of HBSS were injected orthotopically in the left fourth inguinal mammary fat pad and 3 days later, 2.5×10^5 cells in 50 μL of HBSS were injected orthotopically in the right fourth inguinal mammary fat pad. For the lung pseudometastasis model, 5×10^5 E0771 cells in 50 μL of HBSS were injected orthotopically in the left fourth inguinal mammary fat pad and 1 day later, 5×10^5 E0771 cells in 100 μL of HBSS were injected intravenously through the tail vein. Tumor volumes were measured using a digital caliper and calculated using the formula: $V = \pi \times (d^2 \times D)/6$ where d and D are the shortest and longest diameter, respectively. The maximal tumor volume allowed by the Ethical Committee for Animal Experiment of the Vrije Universiteit Brussel is 2000 mm³, which was not exceeded in this study. Mice were randomized when tumor volumes reached ≈ 50–100 mm³ and received the intratumoral injection of vehicle/mRNA-formulated LNP on the same day or 24 h later in case of depletion studies.
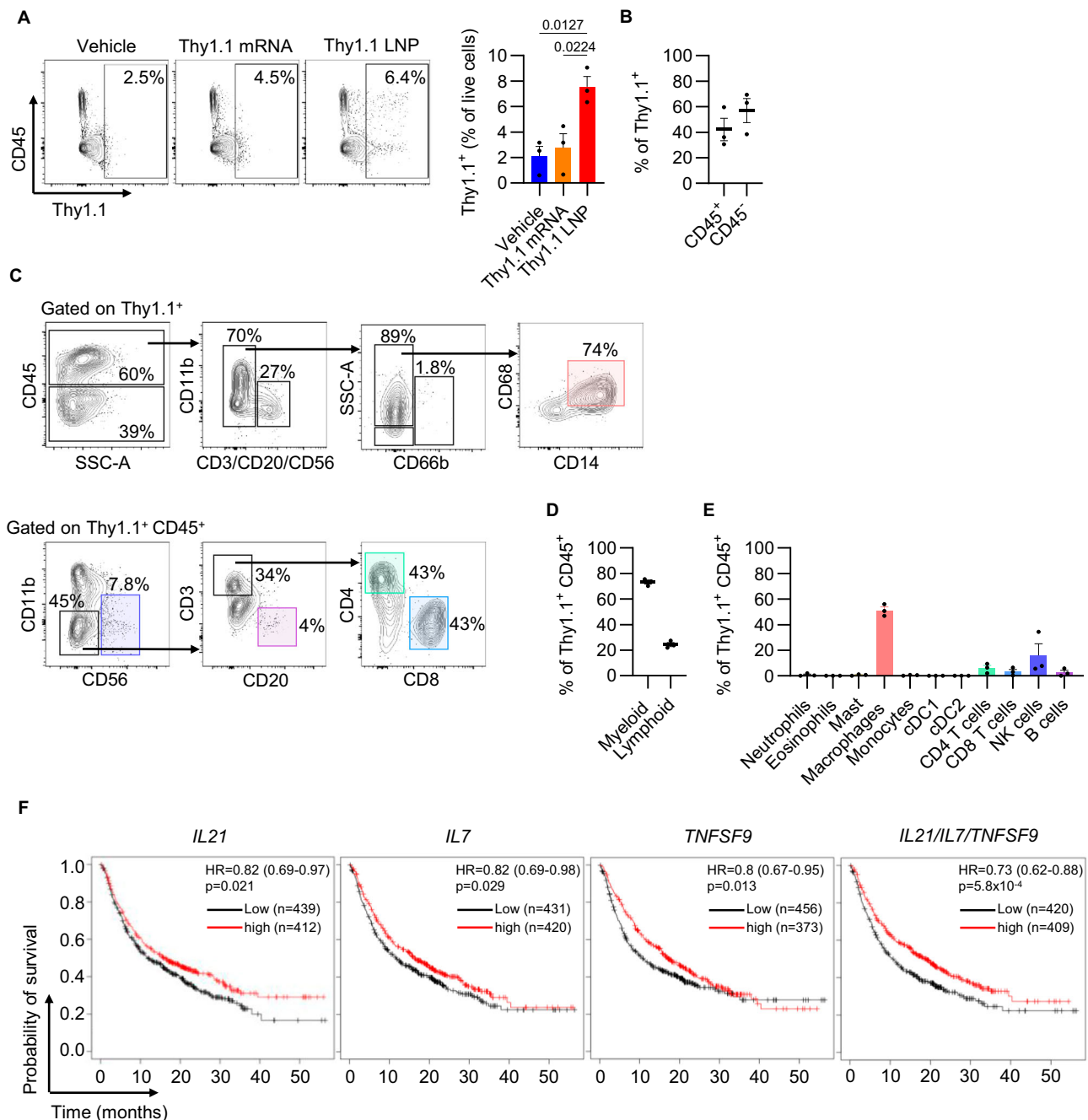
Fig. 8 | LNP-formulated mRNA leads to efficient protein expression in human cells. A Representative flow cytometry plots and bar graph show the frequency of Thy1.1+ cells in cell suspensions of NSCLC biopsies 18 h post incubation with vehicle, 500 ng/ml naked Thy1.1 mRNA, or 500 ng/ml Thy1.1 LNP ($n = 3$ NSCLC biopsies/group). One-way ANOVA followed by post hoc Tukey's multiple comparisons test was performed. **B** Scatter plot shows the frequency of CD45+ and CD45- cells within Thy1.1+ cells ($n = 3$ NSCLC biopsies). **C** Representative flow cytometry plots show the frequency of Thy1.1+ cells within myeloid and lymphoid lineages. **D** Scatter plot shows the frequency of myeloid and lymphoid cells within Thy1.1+ CD45+ cells ($n = 3$ NSCLC biopsies). **E** Bar graph shows the frequency of immune cell subsets within Thy1.1+ CD45+ cells ($n = 3$ NSCLC biopsies). **F** Kaplan-Meier estimates of overall survival comparing the top (high) and bottom (low) of cancer patients based on the median expression of the indicated genes. Hazard ratio (HR) with 95% confidence interval. p values calculated using log rank test. Tick marks indicate censoring. Bars and horizontal lines show mean. Error bars indicate SEM. Source data for (**A**, **B**, **D**, **E**) are provided as a Source Data file. NSCLC, non-small cell lung carcinoma; SEM, standard error of mean.

Treatments

For Thy1.1 mRNA-formulated LNP and luciferase mRNA-formulated LNP treatments, the mice received a single dose of 15 μg. For IL-21 LNP, IL-7 LNP and 4-1BBL LNP monotherapies, the mice received three doses of 15 μg (5 μg of the respective immunomodulatory agent and 10 μg of a non-translatable form of IL-21 mRNA as a filler) in 20 μL of Tris-Buffered Saline (TBS). For the dual efficacy study, the mice received three doses of 3.33 μg, 6.66 μg or 10 μg each (3.33 μg of IL-21; 3.33 μg of each IL-21 and IL-7; 3.33 μg of each IL-7 and 4-1BBL; 3.33 μg of each IL-21 and 4-1BBL; 3.33 μg of each IL-21, IL-7 and 4-1BBL) in 20 μL of TBS. For the other studies, the mice received three doses of 15 μg each (5 μg of each IL-21, IL-7, and 4-1BBL) in 20 μL of TBS. The second and third doses were administered 3 and 7 days following the first dose. The control LNP contained the same

amount of mRNA that encoded a non-translatable form of IL-21 (ntrIL21 LNP).

For CD8+ T-cell depletion, 200 µg of anti-CD8 antibody (clones 2.43 or YTS 169.4; BioXCell) was intraperitoneally administered in 100 µL of HBSS every 2-3 days starting 1 day before the first vehicle/LNP intratumoral injection. For NK-cell depletion, 300 µg of anti-NK1.1 antibody (clone PK136; BioXCell) was intraperitoneally administered in 100 µL of HBSS every 2-3 days starting 1 day before the first vehicle/LNP intratumoral injection. For neutrophil depletion, mice received 75 µg anti-Ly6G antibody (clone 1A8, BioXCell) intraperitonially every second day, followed by 150 µg of anti-rat immunoglobulin (clone MAR 18.5, BioXCell) intraperitonially 24 h later. For macrophage depletion, the CSF1R inhibitor PLX5622 (HY-114153, MedChemExpress) was administered via rodent chow (1200 mg PLX5622/Kg chow) starting 2 days prior to the first intratumoral injection and until 2 days after the third intratumoral injection. OpenStandard Diet with 15 kcal% fat (control diet) and OpenStandard Diet with 15 kcal% fat and 1200 mg PLX5622/Kg (PLX5622 diet) were prepared by Research Diets, Inc. To block T-cell egression, 60 µg of FTY720 (S5002; Selleck Chemicals) was intraperitoneally administered in 100 µL of 0.9% (w/v) NaCl daily starting 1 day before the first vehicle/LNP intratumoral injection. For anti-PD1 treatment, 200 µg of anti-PD1 (clone RMP1-14; BioXCell) was intraperitoneally administered in 100 µL of HBSS on day 10, 13, 17 and 20 post E0771 inoculation.

Blood collection and tissue dissociation

Blood was collected from mice through the tail or submandibular vein and transferred into a tube containing HBSS supplemented with 2 mM EDTA and 0.5% (v/v) FCS. Tumors and tdLNs were isolated, cut into small pieces, and digested with 10 U/mL collagenase I, 400 U/mL collagenase IV, and 30 U/mL DNase I (Worthington) in Roswell Park Memorial Institute (RPMI) 1640 medium for 20 min at 37 °C with constant mixing. Tumors were further triturated and filtered through a 70 µm cell strainer while tdLNs were only filtered through a 70 µm cell strainer. Spleens were mechanically dissociated against a 70 µm cell strainer. Bone marrow was flushed out of the tibia and femur using a 27 G needle filled with RPMI. Livers were perfused with 10 ml HBSS through the *vena cava*, isolated, transferred into gentleMACS C tubes (Miltenyi Biotech) and cut into small pieces using the gentleMACS dissociator (Miltenyi Biotech). Then, livers were digested for 30 min at 37 °C using 1 mg/mL collagenase A and 10 U/mL DNase (Roche). NSCLC biopsies were cut into small pieces, and digested with 10 U/mL collagenase I, 400 U/mL collagenase IV, and 30 U/mL DNase I (Worthington) in RPMI 1640 medium for 30 min at 37 °C with constant mixing. NSCLC samples were further triturated and filtered through a 70 µm cell strainer. Single cell suspensions were then treated with ammonium-chloride-potassium (ACK) erythrocyte lysis buffer.

Flow cytometry

Single cell suspensions were resuspended in HBSS containing BD Horizon Fixable Viability Stain 575 V (1:2000; BD Biosciences) and incubated for 15 min at room temperature. Next, cell suspensions were washed with and resuspended in HBSS supplemented with 2 mM ethylenediaminetetraacetic acid (EDTA) and 0.5% (v/v) FCS. Cells were preincubated with anti-CD16/CD32 antibody (clone 2.4G2) for 10 min on ice to prevent nonspecific antibody binding to Fcγ receptors. Next, cell suspensions were incubated with fluorochrome-conjugated antibodies diluted in HBSS supplemented with 2 mM EDTA and 0.5% (v/v) FCS for 30 min at 4 °C and then washed with the same buffer.

For intracellular staining, cells were fixed after extracellular staining using the FoxP3 Intracellular Fixation and Permeabilization Buffer Set (Thermo Fisher Scientific, 88-8824-00) according to the manufacturer's instructions. The fluorochrome-conjugated antibodies used for extracellular and intracellular staining are listed in Supplementary Table 2.

For staining IFN-γ and TNF-α, tumor cell suspensions were pre-incubated in RPMI 1640 (Gibco) supplemented with 10% (v/v) heat-inactivated FCS (Capricorn Scientific), 300 µg/mL L-glutamine, 100 units/mL penicillin, 100 µg/mL, streptomycin, 1 mM non-essential amino acids, 1 mM sodium pyruvate, 0.02 mM 2-mercapto ethanol, 5 µg/mL Brefeldin A (BioLegend), 20 ng/ml phorbol 12-myristate 13-acetate (PMA; Sigma-Aldrich), and 1 µg/ml ionomycin (Invitrogen) for 5 h to stimulate NK and T cells.

Flow cytometry data were acquired using BD FACSCanto II (BD Biosciences) or BD FACS Symphony A3 (BD Biosciences) and analyzed using FlowJo.

Tumor and serum cytokine measurement and Liver damage-associated enzymes

Tumors were cut into small pieces in RPMI and the supernatant was collected and centrifuged at $14,000 \times g$ for 5 min to remove insoluble material. Blood was centrifuged at $1000 \times g$ for 15 min and serum was collected. Tumor supernatant and serum were frozen at −20 °C until use. IL-21 and IL-7 levels were quantified using the Mouse IL-21 DuoSet ELISA kit (DY594, R&D Systems) and Mouse IL-7 DuoSet ELISA kit (DY407, R&D Systems), respectively, according to the manufacturer's instructions. Clear Polystyrene Microplates, ELISA Plate Sealers, TMB ELISA Substrate, Stop Solution, ELISA Plate-coating Buffer, Reagent Diluent Concentrate, and Wash Buffer were all provided in the DuoSet ELISA Ancillary Reagent Kit 2 (DY008B, R&D Systems) and used according to the manufacturer's instructions. AST/ALT activity was measured on serum samples using an AST Activity assay kit (MAK055-1KT, Merck) or an ALT Activity assay kit (MAK052, Merck) according to the manufacturer's instructions.

Liver immunohistochemistry

Livers were perfused with 10 ml HBSS through the *vena cava*, isolated and fixed in 4% formaldehyde for 24 h at room temperature. Then, they were washed 3x with PBS and stored at 4 °C until further use. Liver tissues were embedded in paraffin and cut into 5 µm sections. Hematoxylin-eosin staining was performed automatically using the Sakura Tissue-Tek Prisma. Briefly, the tissues were consecutively stained using hematoxylin Gill II (Sigma), Nu-Clear II (Thermo Fisher), Erythrosine B-sodium salt (Sigma) and Bluing Reagent (Thermo Fisher). Tissue sections were scored for signs of inflammation and cell death by a pathologist. Picrosirius staining was performed manually by first incubating the tissue sections for 10 min in 100% methanol followed by 1 h at room temperature in Sirius Green solution containing Sirius Red (Sigma) and Fast Green FCF (Sigma) dissolved in saturated picric acid (VWR). Tissue sections were scored for signs of fibrosis by a pathologist. Images were acquired using the EVOS M7000 microscope (Thermo Fisher Scientific).

In vivo bioluminescence imaging

For in vivo imaging, mice were sedated with isoflurane and inoculated subcutaneously with 5×10^5 MC38 cells. When tumor volume reached 50–100 mm³, 10 µg of naked mRNA or LNP-formulated mRNA coding for Fluc was injected into the tumor. To monitor Fluc activity, 100 µl of 30 mg/ml D-luciferin (E1605, Promega) in 0.9% Potassium salt solution was injected intraperitoneally at different time points after mRNA/LNP injection. Images were taken 10–15 min after injection of luciferin to reach the emission peak. The mice were sedated and monitored using an IVIS Lumina II imaging system. Photon flux was quantified using the Living Image 4.4 software (all from Caliper Life Sciences, Hopkinton, MA, USA). Regions of interest (ROIs) were quantified as average radiance (photons/[s cm2 sr]) or total flux (photons s-1) represented as color-scaled images superimposed on grayscale photos of mice using Living Image software (Caliper Life Sciences).

Cellular indexing of transcriptome and epitopes by sequencing (CITE-Seq)

The tumors and tdLNs were processed as previously described with the addition of actinomycin D (A1410-5MG, Sigma-Aldrich) to collection and processing buffers. Tumors and tdLNs were collected in the presence of 30 μmol/L actinomycin D. The digestion and filtering were done in the presence of 15 μmol/L actinomycin D. All subsequent steps were performed in the presence of 3 μmol/L actinomycin D. Tumors from seven Triplet LNP-treated mice were individually processed and the frequency of CD8$^+$ T cells was determined using flow cytometry. Five tumors with high CD8$^+$ T cell frequency (responders) and their respective tdLNs were pooled. For vehicle- and control LNP-treated mice, five tumors and their respective tdLNs were pooled irrespective of the CD8$^+$ T-cell frequency. Then, 10^6 cells were resuspended in 25 μL of staining mix in 0.04% BSA-PBS containing APC-Cy7-labeled mouse anti-CD45 and the mouse cell surface protein antibody panel containing 151 oligo-conjugated antibodies (Supplementary Table 3; the CITE-seq antibody cocktail used in this study can be purchased from the VIB Single Cell core, Ghent, Belgium).

Next, cells were washed, stained with 7-AAD, and 7-AAD$^-$ CD45$^+$ cells were sorted using BD FACSAria II (BD Biosciences). Then, the 10x genomics single-cell bead-in emulsions and scRNA-seq and CITE-seq libraries were prepared as described previously[61]. The Cell Ranger software (10x Genomics) v.6.0.0 was used to perform alignment of the RNA sequencing reads to the reference genome (Mus musculus GRCm38) and generation of the RNA and ADT UMI count matrices. The average mean number of mapped RNA reads per cell was 22 171 ± 4473 SD, with an average sequencing saturation metric of 44.97% ± 10.22% SD. The ADT libraries yielded 2737 ± 713 SD mean reads per cell, with 79.62% ± 6.05% SD sequencing saturation. Further preprocessing and analysis of the UMI count matrices were performed in R using Seurat v.4.0.5, DropletUtils v1.10.3, scater v.1.22.0, scDblFinder v.1.8.0. The cellular barcodes, associated with low quality empty droplets, were filtered out using the emptyDrops function of the DropletUtils package with the recommended FDR cutoff <= 0.1 for deviation from the ambient RNA profile. A doublet score was assigned to each cell barcode based on the generation of cluster-based artificial doublets with the scDblFinder function of the scDblFinder package. The gene expression matrices were further filtered for low-quality cells, normalized, and scaled, followed by the selection of highly variable genes, principal components analysis, and clustering as previously described[62]. The genes, specifically expressed in each cluster, were identified via differential expression analysis with the FindMarkers function of Seurat (Wilcoxon Rank Sum test). The *p*-values of differential expression were adjusted for multiple testing with Bonferroni correction. Clustering results were visualized using two-dimensional scatter plots with the Uniform Manifold Approximation and Projection (UMAP) method.

The processing of the ADT expression matrix was done as described previously[62]. In brief, the ADT cell barcodes, associated with artifact cells based on the RNA expression analysis were discarded, and the remaining data was normalized using the ASINH_GEOM transformation (inverse hyperbolic sine transformation with a cofactor).

For the analysis of the T-cell subsets of the tumor and tdLN samples, the weighted-nearest neighbor method of the Seurat package has been applied. First, preprocessing was performed on the RNA and the ADT matrices independently, including standard normalization, scaling, highly variable genes' selection (for the RNA matrix only), and principal components analysis. Then, the closest neighbors of each cell are calculated based on weighted combinations of the RNA and protein signal similarities in the PCA space. The calculated weighted nearest neighbors (WNN) graph is used downstream for UMAP dimensionality reduction and clustering using the smart local moving (SLM) algorithm.

To perform gene ontology (GO) enrichment analysis on the CD8T Prf1 Lag3 hi, we compiled a list of the upregulated genes (Fold change>0.5, adjusted *p* value < 0.05) in this cluster in comparison to other T cell clusters. Then, we utilized the clusterProfiler R package (v 4.1)[63] and the org.Mm.eg.db v3.18 to generate and visualize gene functional annotation.

Modeling the intercellular communication using NicheNet

For predicting interactions between the myeloid cells and the CD8$^+$ T cells, we applied the Differential NicheNet approach of the NicheNet R package (v. 1.1.1), using the pre-build NicheNet prior model of ligand-receptor and ligand-target interactions. More specifically, we investigated the cell-cell communication differences of tumors/tdLN from Triplet LNP-treated mice versus those from control mice (Vehicle- and Control LNP-treated). Tumor-derived monocytes, macrophages, neutrophils, and cDCs or tdLN cDCs were defined as senders, while CD8$^+$ T cells in the tumor or lymph node were defined as the receiver cell population.

First, differential expression (DE) was calculated for each pairwise sender cell type comparison between the conditions (e.g., treated neutrophils versus control neutrophils, treated neutrophils versus control cDC2, etc.). DE was also assessed in the receiver cell type between the conditions. For summarizing the DE results, the minimal logFC value was used for DE genes from each sender/receiver cell type, which were also present in the prior ligand-receptor model. Using the minimum logFC statistic allows prioritizing potential ligands/receptors that are more strongly expressed in the cell type of the treatment condition compared to all cell types of the controls.

Next, the ligand activities of each ligand for each of the receiver cell types and in each of the two conditions were predicted. To that end, the potential ligands were ranked based on the presence of their target genes in the gene set of interest (DE genes in the receiver between the treated and the control condition, logFC>0.15), compared to a background set of genes. To predict active, affected targets of the potential ligands, only a gene set of interest genes were considered, that also belong to the a priori top 250 targets of a ligand. Finally, a cumulative prioritization score was calculated for each ligand-receptor and ligand-target link, using a weighted sum of the scaled scores of the ligand activity, average expression, and fraction of expression of ligands, receptors, and target genes across all cell types of interest, and whether the interaction is documented in curated databases ('bona fide'), or is predicted based on gene annotation and protein-protein interaction databases.

Generation and polarization of bone marrow-derived macrophages (BMDMs)

BMDM generation was performed as described previously[64]. Bone marrow cells were cultured for 13 days in RPMI-1640 medium supplemented with 300 μg/ml L-glutamine, 100 mg/ml streptomycin, 100 units/ml penicillin, 20% (v/v) heat-inactivated FCS (Capricorn Scientific) and 30% L929-conditioned medium. Subsequently, BMDMs were harvested and plated at a concentration of 10^6 cells/ml in RPMI-1640 medium supplemented with 300 μg/ml L-glutamine, 100 mg/ml streptomycin, 100 units/ml penicillin, 10% (v/v) heat-inactivated FCS (Capricorn Scientific). Next, BMDMs were stimulated with either 100 ng/ml LPS (Sigma-Aldrich) or 100 ng/ml IL-4 (Z02996-50, GenScript). Macrophage polarization was assessed by flow cytometry.

Enzyme-linked immunosorbent spot (ELISpot)

Seven days after the third intratumoral injection, spleens were isolated and dissociated into single cell suspension. IFN-γ producing tumor cells were detected using an IFN-γ ELISpot kit (Diaclone Murine IFNγ ELISpot Set) following the supplier's protocol. For peptide stimulation, total splenocytes from mice were incubated with 10 μg of p15E

(KSPWFTTL) peptide. The IFN-γ spots were enumerated using an automated ImmunoSpot analyzer (Cellular Technology Ltd).

Survival analysis of patients with cancer

The survival analysis was performed using the survival analysis tool KM plotter – immunotherapy[46]. Using their tool, we split the patients that did not receive immunotherapy (n = 976) regardless of their sex by the median expression of the indicated genes and assessed the overall survival. The dataset used included bladder carcinoma, esophageal adenocarcinoma, glioblastoma, hepatocellular carcinoma, head and neck squamous cell carcinomas, melanoma, non-small cell lung carcinoma, and urothelial carcinoma patients.

Statistical analysis

Statistical analyses were performed using GraphPad Prism 9.1.2 software.

Reporting summary

Further information on research design is available in the Nature Portfolio Reporting Summary linked to this article.

Data availability

The CITE-seq raw data generated in this study has been deposited in the GEO database (NCBI) under accession code GSE249674. Survival analysis of cancer patients was performed using the survival analysis web-based tool KM plotter – immunotherapy [https://kmplot.com/analysis/index.php?p=service&cancer=immunotherapy]. The remaining data are available within the Article, Supplementary Information or Source Data file. Source data are provided with this paper.

References

1. Qin, S. et al. mRNA-based therapeutics: powerful and versatile tools to combat diseases. *Signal Transduct. Target. Ther.* **7**, 166 (2022).
2. Beck, J. D. et al. mRNA therapeutics in cancer immunotherapy. *Mol. Cancer* **20**, 69 (2021).
3. Van Lint, S. et al. Intratumoral Delivery of TriMix mRNA Results in T-cell Activation by Cross-Presenting Dendritic Cells. *Cancer Immunol. Res.* **4**, 146–156 (2016).
4. Hotz, C. et al. Local delivery of mRNA-encoding cytokines promotes antitumor immunity and tumor eradication across multiple pre-clinical tumor models. *Sci. Transl. Med.* **13**, eabc7804 (2021).
5. Hewitt, S. L. et al. Intratumoral IL12 mRNA Therapy Promotes TH1 Transformation of the Tumor Microenvironment. *Clin. Cancer Res.* **26**, 6284–6298 (2020).
6. Hewitt, S. L. et al. Durable anticancer immunity from intratumoral administration of IL-23, IL-36γ, and OX40L mRNAs. *Sci. Transl. Med.* **11**, eaat9143 (2019).
7. Huang, X. et al. The landscape of mRNA nanomedicine. *Nat. Med.* **28**, 2273–2287 (2022).
8. Hou, X., Zaks, T., Langer, R. & Dong, Y. Lipid nanoparticles for mRNA delivery. *Nat. Rev. Mater.* **6**, 1078–1094 (2021).
9. Bevers, S. et al. mRNA-LNP vaccines tuned for systemic immunization induce strong antitumor immunity by engaging splenic immune cells. *Mol. Ther.* **30**, 3078–3094 (2022).
10. Leonard, W. J. & Wan, C. K. IL-21 Signaling in Immunity. *F1000Research* **5**, (F1000 Faculty Rev):224 (2016).
11. Moroz, A. et al. IL-21 Enhances and Sustains CD8+ T Cell Responses to Achieve Durable Tumor Immunity: Comparative Evaluation of IL-2, IL-15, and IL-211. *J. Immunol.* **173**, 900–909 (2004).
12. Søndergaard, H. et al. Intratumoral Interleukin-21 Increases Antitumor Immunity, Tumor-infiltrating CD8+ T-cell Density and Activity, and Enlarges Draining Lymph Nodes. *J. Immunother.* **33**, 236–249 (2010).
13. Skak, K., Søndergaard, H., Frederiksen, K. S. & Ehrnrooth, E. In vivo antitumor efficacy of interleukin-21 in combination with chemotherapeutics. *Cytokine* **48**, 231–238 (2009).
14. Seo, H. et al. IL21 Therapy Combined with PD-1 and Tim-3 Blockade Provides Enhanced NK Cell Antitumor Activity against MHC Class I–Deficient Tumors. *Cancer Immunol. Res.* **6**, 685–695 (2018).
15. Chen, T. et al. IL-21 arming potentiates the anti-tumor activity of an oncolytic vaccinia virus in monotherapy and combination therapy. *J. Immunother. Cancer* **9**, e001647 (2021).
16. Li, Y. et al. CCL21/IL21-armed oncolytic adenovirus enhances antitumor activity against TERT-positive tumor cells. *Virus Res.* **220**, 172–178 (2016).
17. Bhatt, S. et al. Anti-CD20-interleukin-21 fusokine targets malignant B cells via direct apoptosis and NK-cell–dependent cytotoxicity. *Blood* **129**, 2246–2256 (2017).
18. Thompson, J. A. et al. Phase I study of recombinant interleukin-21 in patients with metastatic melanoma and renal cell carcinoma. *J. Clin. Oncol.* **26**, 2034–2039 (2008).
19. Berraondo, P. et al. Cytokines in clinical cancer immunotherapy. *Br. J. Cancer* **120**, 6–15 (2019).
20. Schluns, K. S., Kieper, W. C., Jameson, S. C. & Lefrançois, L. Interleukin-7 mediates the homeostasis of naïve and memory CD8 T cells in vivo. *Nat. Immunol.* **1**, 426–432 (2000).
21. Tan, J. T. et al. IL-7 is critical for homeostatic proliferation and survival of naïve T cells. *Proc. Natl. Acad. Sci.* **98**, 8732–8737 (2001).
22. Kieper, W. C. et al. Overexpression of Interleukin (IL)-7 Leads to IL-15–independent Generation of Memory Phenotype CD8+ T Cells. *J. Exp. Med.* **195**, 1533–1539 (2002).
23. Lynch, D. H., Namen, A. E. & Miller, R. E. In vivo evaluation of the effects of interleukins 2, 4 and 7 on enhancing the immunotherapeutic efficacy of anti-tumor cytotoxic T lymphocytes. *Eur. J. Immunol.* **21**, 2977–2985 (1991).
24. Koyas, A. et al. Interleukin-7 protects CD8+ T cells from adenosine-mediated immunosuppression. *Sci. Signal.* **14**, eabb1269 (2021).
25. Rosenberg, S. A. et al. IL-7 Administration to Humans Leads to Expansion of CD8+ and CD4+ Cells but a Relative Decrease of CD4+ T-Regulatory Cells. *J. Immunother.* **29**, 313–319 (2006).
26. Sportès, C. et al. Administration of rhIL-7 in humans increases in vivo TCR repertoire diversity by preferential expansion of naive T cell subsets. *J. Exp. Med.* **205**, 1701–1714 (2008).
27. Lee, K.-J. et al. IL-7-primed bystander CD8 tumor-infiltrating lymphocytes optimize the antitumor efficacy of T cell engager immunotherapy. *Cell Rep. Med.* **5**, 101567 (2024).
28. Kim, A. M. J., Nemeth, M. R. & Lim, S.-O. 4-1BB: A promising target for cancer immunotherapy. *Front. Oncol.* **12**, 968360 (2022).
29. Seong, A. J., Sang-Min, P., Sang-Chul, L., Byoung, S. K. & Byung-Sam, K. Marked Expansion of CD11c+CD8+ T-Cells in Melanoma-bearing Mice Induced by Anti-4-1BB Monoclonal Antibody. *Molecules Cells* **24**, 132–138 (2007).
30. Ju, S.-A. et al. Immunity to melanoma mediated by 4-1BB is associated with enhanced activity of tumour-infiltrating lymphocytes. *Immunol. Cell Biol.* **83**, 344–351 (2005).
31. Segal, N. H. et al. Results from an Integrated Safety Analysis of Urelumab, an Agonist Anti-CD137 Monoclonal Antibody. *Clin. Cancer Res.* **23**, 1929–1936 (2017).
32. Segal, N. H. et al. Phase I Study of Single-Agent Utomilumab (PF-05082566), a 4-1BB/CD137 Agonist, in Patients with Advanced Cancer. *Clin. Cancer Res.* **24**, 1816–1823 (2018).
33. De Lombaerde, E. et al. Combinatorial Screening of Biscarbamate Ionizable Lipids Identifies a Low Reactogenicity Lipid for Lipid Nanoparticle mRNA Delivery. *Adv. Funct. Mater.* **34**, 2310623 (2024).
34. Lamoot, A. et al. Successful batch and continuous lyophilization of mRNA LNP formulations depend on cryoprotectants and ionizable lipids. *Biomater. Sci.* **11**, 4327–4334 (2023).

35. Di, J. et al. Biodistribution and Non-linear Gene Expression of mRNA LNPs Affected by Delivery Route and Particle Size. *Pharm. Res.* **39**, 105–114 (2022).

36. Zeng, R. et al. Synergy of IL-21 and IL-15 in regulating CD8+ T cell expansion and function. *J. Exp. Med.* **201**, 139–148 (2005).

37. Gu, Y.-Z. et al. Forced co-expression of IL-21 and IL-7 in whole-cell cancer vaccines promotes antitumor immunity. *Sci. Rep.* **6**, 32351 (2016).

38. Liu, S. et al. IL-21 synergizes with IL-7 to augment expansion and anti-tumor function of cytotoxic T cells. *Int. Immunol.* **19**, 1213–1221 (2007).

39. Wang, X. et al. Immunological therapy: A novel thriving area for triple-negative breast cancer treatment. *Cancer Lett.* **442**, 409–428 (2019).

40. Bartkowiak, T. et al. Activation of 4-1BB on Liver Myeloid Cells Triggers Hepatitis via an Interleukin-27-Dependent Pathway. *Clin. cancer Res.* **24**, 1138–1151 (2018).

41. Yamauchi, T. et al. T-cell CX3CR1 expression as a dynamic blood-based biomarker of response to immune checkpoint inhibitors. *Nat. Commun.* **12**, 1402 (2021).

42. Pauken, K. E. et al. Single-cell analyses identify circulating anti-tumor CD8 T cells and markers for their enrichment. *J. Exp. Med.* **218**, e20200920 (2021).

43. Andreatta, M. et al. Interpretation of T cell states from single-cell transcriptomics data using reference atlases. *Nat. Commun.* **12**, 2965 (2021).

44. Gungabeesoon, J. et al. A neutrophil response linked to tumor control in immunotherapy. *Cell* **186**, 1448–1464.e1420 (2023).

45. Di Pilato, M. et al. CXCR6 positions cytotoxic T cells to receive critical survival signals in the tumor microenvironment. *Cell* **184**, 4512–4530.e4522 (2021).

46. Kovács, S. A., Fekete, J. T. & Győrffy, B. Predictive biomarkers of immunotherapy response with pharmacological applications in solid tumors. *Acta Pharmacologica Sin.* **44**, 1879–1889 (2023).

47. Connors, J. et al. Lipid nanoparticles (LNP) induce activation and maturation of antigen presenting cells in young and aged individuals. *Commun. Biol.* **6**, 188 (2023).

48. Zeng, Y., Escalona-Rayo, O., Knol, R., Kros, A. & Slütter, B. Lipid nanoparticle-based mRNA candidates elicit potent T cell responses. *Biomater. Sci.* **11**, 964–974 (2023).

49. Zhang, Y. et al. Immunotherapy of Tumor RNA-Loaded Lipid Nanoparticles Against Hepatocellular Carcinoma. *Int. J. Nanomed.* **16**, 1553–1564 (2021).

50. Chen, D. S. & Mellman, I. Oncology meets immunology: the cancer-immunity cycle. *Immunity* **39**, 1–10 (2013).

51. Roberts, E. W. et al. Critical Role for CD103+/CD141+ Dendritic Cells Bearing CCR7 for Tumor Antigen Trafficking and Priming of T Cell Immunity in Melanoma. *Cancer Cell* **30**, 324–336 (2016).

52. Binnewies, M. et al. Unleashing Type-2 Dendritic Cells to Drive Protective Antitumor CD4+ T Cell Immunity. *Cell* **177**, 556–571.e516 (2019).

53. Hong, W. X. et al. Intratumoral Immunotherapy for Early-stage Solid Tumors. *Clin. Cancer Res.* **26**, 3091–3099 (2020).

54. Li, F. et al. The association between CD8+ tumor-infiltrating lymphocytes and the clinical outcome of cancer immunotherapy: A systematic review and meta-analysis. *EClinicalMedicine* **41**, 101134 (2021).

55. Chamucero-Millares, J. A., Bernal-Estévez, D. A. & Parra-López, C. A. Usefulness of IL-21, IL-7, and IL-15 conditioned media for expansion of antigen-specific CD8+ T cells from healthy donor-PBMCs suitable for immunotherapy. *Cell. Immunol.* **360**, 104257 (2021).

56. Hashimoto-Kataoka, T. et al. Interleukin-6/interleukin-21 signaling axis is critical in the pathogenesis of pulmonary arterial hypertension. *Proc. Natl Acad. Sci.* **112**, E2677–E2686 (2015).

57. Miki, H., Han, K. H., Scott, D., Croft, M. & Kang, Y. J. 4-1BBL Regulates the Polarization of Macrophages, and Inhibition of 4-1BBL Signaling Alleviates Imiquimod-Induced Psoriasis. *J. Immunol.* **204**, 1892–1903 (2020).

58. Prokhnevska, N. et al. CD8+ T cell activation in cancer comprises an initial activation phase in lymph nodes followed by effector differentiation within the tumor. *Immunity* **56**, 107–124.e5 (2022).

59. Connolly, K. A. et al. A reservoir of stem-like CD8+ T cells in the tumor-draining lymph node preserves the ongoing antitumor immune response. *Sci. Immunol.* **6**, eabg7836 (2021).

60. Yamauchi, T. et al. CX3CR1-CD8+ T cells are critical in antitumor efficacy but functionally suppressed in the tumor microenvironment. *JCI insight* **5**, e133920 (2020).

61. Pombo Antunes, A. R. et al. Single-cell profiling of myeloid cells in glioblastoma across species and disease stage reveals macrophage competition and specialization. *Nat. Neurosci.* **24**, 595–610 (2021).

62. Scheyltjens, I. et al. Single-cell RNA and protein profiling of immune cells from the mouse brain and its border tissues. *Nat. Protoc.* **17**, 2354–2388 (2022).

63. Wu, T. et al. clusterProfiler 4.0: A universal enrichment tool for interpreting omics data. *Innovation* **2**, 100141 (2021).

64. Geeraerts, X. et al. Macrophages are metabolically heterogeneous within the tumor microenvironment. *Cell Rep.* **37**, 110171 (2021).

Acknowledgements

Author contributions

Conceptualization: A.E.I.H., S.D.K., F.L., D.L. Investigation: A.E.I.H., J.F., E.B., A.D., J.B., L.J., P.M.R.B., E.K., L.A., M.G., I.V., M.C., E.J.C., F.C., A.A.C., A.G.P., L.F., E.H., M.E.S., R.S., S.D. Formal analysis: A.E.I.H., J.F., E.B., D.K., E.K., P.L., M.G., L.Av.G. Providing human samples: F.A.N. Visualization: A.E.I.H., J.F., D.K., B.G.D.G. Writing – original draft: A.E.I.H. Writing – review and editing: A.E.I.H., F.L., D.L. with input of all authors. Supervision: F.L., D.L. Funding acquisition: S.D.K., B.G.D.G., F.L., D.L.

Competing interests

Additional information

Supplementary information The online version contains supplementary material available at https://doi.org/10.1038/s41467-024-54877-9.

Correspondence and requests for materials should be addressed to Florence Lambolez or Damya Laoui.

Peer review information *Nature Communications* thanks Zhiliang Bai, Alvaro Teijeira, Xiaoyang Xu and the other, anonymous, reviewer(s) for their contribution to the peer review of this work. A peer review file is available.

Reprints and permissions information is available at http://www.nature.com/reprints

Publisher's note Springer Nature remains neutral with regard to jurisdictional claims in published maps and institutional affiliations.

[1]Lab of Dendritic Cell Biology and Cancer Immunotherapy, VIB Center for Inflammation Research, Brussels, Belgium. [2]Lab of Cellular and Molecular Immunology, Brussels Center for Immunology, Vrije Universiteit Brussel (VUB), Brussels, Belgium. [3]etherna, Ghent, Belgium. [4]Liver Cell Biology Research Group, Vrije Universiteit Brussel (VUB), Brussels, Belgium. [5]Department of Anatomo-Pathology, Universitair Ziekenhuis Brussel (UZB), Brussels, Belgium. [6]Department of Pharmaceutics, University of Ghent, Ghent, Belgium. [7]Myeloid Cell Immunology Lab, VIB Center for Inflammation Research, Brussels, Belgium. [8]Laboratory of Tumor Immunology and Immunotherapy, Department of Oncology, Leuven Cancer Institute, KU Leuven, Leuven, Belgium. [9]CDL Research, University Medical Center, Utrecht, The Netherlands. [10]Institut de Duve, Université Catholique de Louvain, Brussels, Belgium. [11]Service de Pneumologie, Cliniques Universitaires Saint-Luc, Brussels, Belgium. [12]These authors contributed equally: Jessica Filtjens, Elisabeth Brabants. [13]These authors jointly supervised this work: Florence Lambolez, Damya Laoui. ✉e-mail: florence.lambolez@etherna.be; dlaoui@vub.be